MAXIMUM RATE OF GROWTH OF ENSTROPHY IN THE NAVIER-STOKES SYSTEM ON 2D BOUNDED DOMAINS

MAXIMUM RATE OF GROWTH OF ENSTROPHY IN THE NAVIER-STOKES SYSTEM ON 2D BOUNDED DOMAINS

By

ADAM ANDRZEJ SLIWIAK, B. Sc.

A Thesis

Submitted to the School of Graduate Studies

in Partial Fulfillment of the Requirements

for the Degree

of Master of Science

McMaster University

MASTER OF SCIENCE (2017) McMaster University

(Computational Science and Engineering) Hamilton, Ontario

TITLE: MAXIMUM RATE OF GROWTH OF ENSTROPHY IN THE NAVIER-STOKES SYSTEM ON 2D BOUNDED DOMAINS

AUTHOR: Adam A. Sliwiak, B. Sc. (Warsaw University of Technology)

SUPERVISOR: Dr. Bartosz Protas

NUMBER OF PAGES: viii, 66

Lay Abstract

For many decades, scientists have been investigating fundamental aspects of the Navier-Stokes equation, a central mathematical model arising in fluid mechanics. Although the equation is widely used by engineers to describe numerous flow phenomena, it is still an open question whether the Navier-Stokes system *always* admits physically meaningful solutions. To address this issue, we want to explore its mathematical aspects deeper by analyzing the behaviour of the enstrophy, which is a quantity associated with the vorticity of the flow and a convenient measure of the regularity of the solution. In this study, we consider a planar and incompressible flow bounded by solid walls. Using basic tools of mathematical analysis and optimization theory, we propose a computational method enabling us to find out how much enstrophy can such a flow produce instantaneously. We present numerical evidence that this instantaneous growth of enstrophy has a well-defined asymptotic behavior, which is consistent with physical assumptions.

Abstract

One of the key open problems in the field of theoretical fluid mechanics concerns the possibility of the singularity formation in solutions of the 3D Navier-Stokes system in finite time. This phenomenon is associated with the behaviour of the enstrophy, which is an L_2 norm of the vorticity and must become unbounded if such a singularity occurs. Although there is no blow-up in the 2D Navier-Stokes equation, we would like to investigate how much enstrophy can a planar incompressible flow in a bounded domain produce given certain initial enstrophy. We address this issue by formulating an optimization problem in which the time derivative of the enstrophy serves as the objective functional and solve it using tools of the optimization theory and calculus of variations.

We propose an efficient computational approach which is based on the iterative steepest-ascent procedure. In addition, we introduce an easy-to-implement method of computing the gradient of the objective functional. Finally, we present computational results addressing the key question of this project and provide numerical evidence that the maximum enstrophy growth exhibits the scaling $\mathrm{d}\mathcal{E}/\mathrm{d}t \sim C\mathcal{E}^2$ for $C > 0$ and $\mathcal{E}_0 \to \infty$. All computations are performed using the Chebyshev spectral method.

Acknowledgments

My two-year-long period as a Master's student at McMaster University was one of the most eventful and fruitful chapters of my life. I had the pleasure of meeting fantastic people, in both the School of Computational Science and Engineering and the Department of Mathematics & Statistics, with whom I spent countless hours for casual conversations, scientific discussions and even philosophical deliberations.

First of all, I want to express my sincere gratitude to my supervisor, Dr. Bartosz Protas, who gave me an opportunity to work with him in the field of theoretical fluid mechanics and meticulously guided me through the process of writing this thesis. Moreover, he taught me what it is like to be a good researcher and encouraged me to engage in many extracurricular activities.

Secondly, I would like to thank my fellow students, Alexander Cherniavsky, Kiret Dhindsa and others, who assisted me in governing McMaster University Chapter of SIAM. Without their sacrifice, the chapter would not be where it is now.

I am especially grateful to my dear wife, Monika Sliwiak, for her love, continued support and patience. Her constant help enabled me to pursue my deepest passions and, simultaneously, to preserve work-life balance.

Last but not least, I would like thank the members of the Examination Committee, Dr. Nicholas Kevlahan and Dr. Li Xi, for their valuable comments and suggestions which have led to the improvement of my thesis.

Contents

List of Figures

1 Introduction

This thesis concerns one of the most famous equations of mathematical physics describing the motion of fluids — the Navier-Stokes equation (NSE). For decades, both scientists and engineers have been striving to better understand complex phenomena involving fluid flows. Thorough comprehension of the physics of fluids enables aerospace designers to optimize the shape of different components of a plane wing leading to reduced fuel consumption. The solution of the Navier-Stokes equation is necessary for hemodynamicists to visualize the process of drug delivery in a human body. These are just two examples among many other that show the huge importance of the field of fluid mechanics in the world of advanced technology. Paradoxically, despite of its ubiquity, many aspects of the mathematical nature of NSE are still unexplored. For many years, mathematicians has been trying to answer the question if solutions to NSE in 3D, for a large period of time, are physically justified. This mystery has been promoted by the Clay Institute to the rank of a Millennium Problem and a scientist who manages to provide a rigorous explanation will be awarded a one million dollar prize. A solid proof of the existence of smooth solutions to the three-dimensional incompressible Navier-Stokes equations defined globally in time would mean that the Millennium Problem is solved and would be a major breakthrough in Fluid Mechanics research[7].

As the title indicates, we are interested in the Navier-Stokes system on a bounded domain. For simplicity, the density parameter ρ is assumed to be constant meaning that the flow is incompressible. In the further analysis, the value of ρ will be assumed to be one. The equation also involves another parameter, namely the kinematic viscosity ν. Based on a balance of momentum in Newton's second law and the conservation of mass,

a complete formulation of a 3D Navier-Stokes system can written in the following form:

$$\frac{\partial \mathbf{v}}{\partial t} + (\mathbf{v} \cdot \nabla)\mathbf{v} + \nabla p - \nu \Delta \mathbf{v} = 0 \qquad \text{in } \Omega \subset \mathbb{R}^3, \tag{1a}$$

$$\nabla \cdot \mathbf{v} = 0 \qquad \text{in } \Omega \subset \mathbb{R}^3, \tag{1b}$$

$$\mathbf{v} \cdot \mathbf{n} = \mathbf{v} \cdot \mathbf{s} = 0 \qquad \text{on } \partial\Omega, \tag{1c}$$

$$\mathbf{v}(\mathbf{x}, 0) = \mathbf{v}_0(\mathbf{x}) \qquad \text{in } \Omega \subset \mathbb{R}^3, \tag{1d}$$

where the vector $\mathbf{v} = [u(\mathbf{x}, t), v(\mathbf{x}, t), v(\mathbf{x}, t)]$ and scalar function $p(\mathbf{x}, t)$ respectively denote velocity and pressure, while $\mathbf{x}$ is a 3-dimensional position vector. The symbol Ω represents a 3-dimensional domain, a subset of $\mathbb{R}^3$. Constraint (1b) is a mathematical representation of the incompressibility of a fluid, and boundary condition (1c), through the projection on both the normal unit vector $\mathbf{n}$ and tangential unit vector $\mathbf{s}$, ensures that the velocity vector is zero on the boundary. Finally, since (1a) is a parabolic PDE, we need to provide initial condition (1d) to close the system. The fourth term of (1a) is associated with viscous forces, but in many problems of hydrodynamics there might also appear other effects, such as external forces, e. g., due to gravity. System (1) without both the viscous term ($\nu = 0$) and the boundary condition $\mathbf{v} \cdot \mathbf{s} = 0$ is referred to as the Euler equation.

The Millennium Problem itself does not assume that the domain is bounded. It involves the question if, given $\nu > 0$ and a smooth and divergence-free initial condition $\mathbf{v}_0$, there exist smooth functions $\mathbf{v}$ and $\mathbf{p}$ satisfying (1) excluding boundary conditions. In 1989, Foias and Temam showed in [8] that the solutions to the 2D NSE on a periodic domain are analytic in time, unlike in the 3D case where the solutions turn out to be analytic only for a small (finite) interval of time. It means that there is still no guarantee that even if the initial condition $\mathbf{v}_0$ is smooth, the solution to the 3D NSE is also smooth for

all time. If the magnitude of $\mathbf{v}_0$ is sufficiently small, then unique and smooth solutions are proven to exist for $t \to \infty$. Nevertheless, it is still an open question if smooth initial data with a large magnitude might lead to some form of singularity. There are many different methods of studying this problem, and one of them involves the enstrophy $\mathcal{E}(t)$, which is the L_2-norm of the vorticity function $\boldsymbol{\omega}$,

$$\mathcal{E}(t) = \frac{1}{2} \int_{\Omega} |\boldsymbol{\omega}(\mathbf{x}, t)|^2 \mathrm{d}\Omega, \tag{2}$$

where

$$\boldsymbol{\omega} = \nabla \times \mathbf{v}. \tag{3}$$

The usefulness of this quantity relies of the fact that singularity formation is strictly related to the behavior of the enstrophy. In the same publication [8], Foias and Temam also proved that boundedness of the enstrophy implies regularity of solutions and vice versa. Thus, a mathematical answer, in the form of rigorous estimates, to the question regarding the enstrophy growth is crucial in the study of regularity. Using a variational maximization approach, Lu and Doering showed in 2008 [14] how rapidly the enstrophy can grow in the 3D periodic setting. They concluded that the estimate

$$\frac{\mathrm{d}\mathcal{E}}{\mathrm{d}t} \leq C\mathcal{E}(t)^3 \tag{4}$$

is indeed sharp. One can understand the word "sharpness" as an existence of divergence-free vector fields that saturate a given upper bound. In the literature, there exists a family of analogous results for both the Burgers Equations and 2D Navier-Stokes equation, and the majority of them involve periodic/unbounded domains. Ayala and Protas studied the maximum growth of enstrophy growth in the Burgers Equation in [2], where they used a variational search technique to find extreme solutions. In 2014,

the same researchers [1] performed a careful analysis on a 2D periodic domain, where they studied the maximum palinstrophy growth. This quantity, given by the formula

$$\mathcal{P}(t) = \frac{1}{2}\int_{\Omega} |\nabla\omega(\mathbf{x},t)|^2 \mathrm{d}\Omega, \tag{5}$$

was used instead of enstrophy in the study of the extreme behaviour of the 2D periodic Navier-Stokes equation, since on 2D domains without solid boundaries the enstrophy may only decreased.

Another big question question is what is the upper bound of the enstrophy when the solution evolves over a finite range of time $[0, T]$ and if the existing finite-time estimates are sharp or not. This problem can be mathematically written as follows,

$$\max_{\mathbf{v}_0 \in X(\Omega), \mathcal{E}(0)=\mathcal{E}_0} \mathcal{E}(T), \tag{6}$$

where X denotes some Sobolev space. In 2011, Ayala and Protas computed numerically the enstrophy growth over a finite time for the Burgers Equation [2], and three years later they successfully finished a similar study on a periodic 2D Navier-Stokes system [1], using palinstrophy instead of enstrophy. There remains an open question how the enstrophy $\mathcal{E}(t)$ behaves in the 3D setting.

Based on this short literature review, a related question that arises is what is the maximum enstrophy growth on a bounded domain. What is the impact of the boundaries on the extreme behaviour exhibited by solutions of an equation and what is the effect of the vorticity generation at the solid walls? Can we extrapolate the results obtained for periodic domains to the cases involving boundaries? The role of boundaries in extreme behavior for the Euler equation has been analysed by Hou and Luo in [16]. Their results indicate that the presence of bounded domains may lead to a finite-time blow-up. Is there a similar result for the bounded 3D Navier-Stokes equation? Unfortunately, the

answer is negative and, moreover, there even does not exist any estimates for the maximum enstrophy/palinstrophy growth in lower space dimensions. Although there is no blow-up in the 2D Navier-Stokes system, even on bounded domains, it is still worthwhile to study how much enstrophy can an incompressible flow produce, depending on $\mathcal{E}_0$. In other words, we aim to answer the question what are the upper bounds on the extreme behaviour, as characterized by the instanteneous growth of enstrophy, in 2D Navier-Stokes flows on bounded domains. This is indeed the primary goal of this project, in which we will develop and validate tools enabling us to study such problems on bounded domains with different shapes. Thus, the following chapters of this thesis will address the problem of the maximum enstrophy growth of a two-dimensional Navier-Stokes system that is defined on a bounded domain. This work is computationally-based in the sense that all conclusions rely on numerical results. The proposed numerical algorithm is based on the vorticity transport equation, while the key mathematical tool enabling us to compute $d\mathcal{E}/dt$ involves variational optimization. Numerical calculations are performed using a Chebyshev spectral collocation method, an approach that is suitable for problems defined on bounded domains and, which is very important, guarantees spectral accuracy. Unfortunately, the numerical results will not be verified with analytical estimates, since there seems to be no such estimates available for the problem at hand. Undoubtedly, a derivation of such estimates is one of the major goals for the future research.

The structure of the main part of the thesis is the following: Chapter 2 is devoted to the mathematical aspects of the two-dimensional Navier-Stokes equation, especially in the context of bounded domains, in Chapter 3 we will focus on the analytical tools used to compute the maximum instantaneous enstrophy growth on a bounded domain (that chapter will cover two different approaches of solving our main problem, namely the method of Euler-Lagrange equations and the gradient-based method), the final part of

Chapter 3 includes a careful analysis of the solutions in the limit $\mathcal{E}_0 \to 0$, in chapters 4 and 5 we study specific numerical methods relevant for this project and discuss the most important computational results, respectively, the final remarks and comments regarding the whole project are put together in Chapter 6.

2 2D Navier-Stokes Equation

The system of two-dimensional Navier-Stokes equations describes the dynamics of planar viscous flows and it can mathematically be written exactly like 3D equivalent (1). This section will be devoted to such flows, especially in the context of the streamfunction-vorticity formulation that will turn out to be very convenient in the study of the extreme behaviour.

2.1 Vorticity Transport Equation

In many scientific and engineering applications, however, instead of the velocity, it is more convenient to use the concept of the vorticity $\boldsymbol{\omega}$, defined in (3), which in the case of 2D space, is equivalent to the pseudoscalar ω,

$$\omega = \boldsymbol{\omega} \cdot \mathbf{k} = \nabla^{\perp}\mathbf{v} = \frac{\partial v}{\partial x} - \frac{\partial u}{\partial y}, \tag{7}$$

where $\mathbf{k}$ denotes a unit vector perpendicular to the xy-plane. Based on the above definition and the fact that the flow is incompressible, we can take the curl of (1), and the first term of on left side becomes

$$\nabla \times \frac{\partial \mathbf{v}}{\partial t} = \frac{\partial}{\partial t}(\nabla \times \mathbf{v}) = \frac{\partial \boldsymbol{\omega}}{\partial t}. \tag{8}$$

In the same manner, the last term of the LHS becomes

$$\nabla \times (\nu \Delta \mathbf{v}) = \nu \Delta \boldsymbol{\omega}, \tag{9}$$

while the curl of the pressure gradient vanishes, because p is a scalar function. Moreover, the convection term can be rewritten in the following way,

$$\mathbf{v} \cdot \nabla \mathbf{v} = \frac{1}{2}\nabla(\mathbf{v} \cdot \mathbf{v}) - \mathbf{v} \times (\nabla \times \mathbf{v}) = \nabla \left(\frac{\mathbf{v}^2}{2} \right) - \mathbf{v} \times \boldsymbol{\omega} \tag{10}$$

and, therefore,

$$\begin{aligned} \nabla \times (\mathbf{v} \cdot \nabla \mathbf{v}) &= \nabla \times \nabla \left(\frac{\mathbf{v}^2}{2} \right) - \nabla \times (\mathbf{v} \times \boldsymbol{\omega}) = \nabla \times (\boldsymbol{\omega} \times \mathbf{v}) \\ &= (\mathbf{v} \cdot \nabla)\boldsymbol{\omega} - (\boldsymbol{\omega} \cdot \nabla)\mathbf{v} + \boldsymbol{\omega}(\nabla \cdot \mathbf{v}) + \mathbf{v}(\nabla \cdot \boldsymbol{\omega}). \end{aligned} \tag{11}$$

By incompressibility, the third term of (11) vanishes. The last term also disappears, because a divergence of a curl of any smooth vector is zero. Since we are considering two-dimensional incompressible flows, the second term also goes away. Finally, we can conclude that the evolution equation for the scalar function ω is

$$\frac{\partial \omega}{\partial t} + (\mathbf{v} \cdot \nabla)\omega = \nu \Delta \omega. \tag{12}$$

This parabolic PDE is widely known as the vorticity transport equation and it is also a convection-diffusion type of an equation, which means that the vorticity is both diffused and convected. Unfortunately, there are no boundary conditions for ω, which is troublesome from the computational point of view. In order to surmount this difficulty, it might be helpful to use the concept of the streamfunction. Such a function, denoted by ψ, is related to the velocity field $\mathbf{v}$ by the following identity,

$$\mathbf{v} = \nabla \times \psi \mathbf{k}. \tag{13}$$

which implies that

$$u = \frac{\partial \psi}{\partial y} \quad \text{and} \quad v = -\frac{\partial \psi}{\partial x}. \tag{14}$$

Lines of constant ψ are called streamlines and are tangent to the velocity vector field. The kinematic relation between the streamfunction and the vorticity can be derived using (1b), (7) and (14). Thus, we obtain an elliptic PDE,

$$\Delta \psi = -\omega, \tag{15}$$

that is defined inside the domain Ω. Because of the no-slip boundary conditions for the velocity field, we conclude that the streamfunction satisfies both the homogeneous Dirichlet and Neumann conditions,

$$\psi = \frac{\partial \psi}{\partial n} = 0 \qquad \text{on } \partial\Omega. \tag{16}$$

Equations (12), (15), and (16) lead to the vorticity-streamfunction formulation of 2D Navier-Stokes system (1). One of the biggest advantages of this system is the fact that the solution pair (ω, ψ) automatically satisfies the incompressibility constraint, which means that the corresponding velocity field is divergence-free in both the continuous and discrete setting. Analysing this formulation, we can easily observe the parabolic-elliptic character of NSE. It features two Laplace operators associated with both unknown variables, ω and ψ, and there are two boundary conditions for the streamfunction. The lack of a boundary condition for the vorticity, however, is a source of both analytic and numerical complications, which we will discuss later. Relation (15) and boundary conditions (16) imply zero average property of the vorticity field, which can be shown

by a simple integration by parts,

$$\int_{\Omega} \omega \mathrm{d}\Omega = -\int_{\Omega} \Delta\psi \mathrm{d}\Omega = \oint_{\partial\Omega} \frac{\partial\psi}{\partial n} \mathrm{d}\sigma = 0. \tag{17}$$

To sum up, we can notice that using the concept of the vorticity and the streamfunction, we reduce the NSE system (1) in 2D space to equations (12), (15) with boundary conditions (16). Once the vorticity-streamfunction system is solved, the velocity can be computed by taking appropriate partial derivatives of the streamfunction. It is more complicated to retrieve the pressure, since one has to solve the Pressure Poisson Equation (PPE) with suitable boundary conditions, and this will be discussed in the next section.

2.2 Pressure Poisson Equation

In our further derivations, we will need different relations between the pressure and vorticity (or streamfunction) and, therefore, we would like to take a closer look at the former. To determine the pressure, we should take the divergence of momentum equation (1a). Such manipulation leads to the following Pressure Poisson Equation (PPE) equation,

$$\Delta p = -\nabla \cdot [(\mathbf{v} \cdot \nabla)\mathbf{v}] = 2\left(\frac{\partial u}{\partial x}\frac{\partial v}{\partial y} - \frac{\partial u}{\partial y}\frac{\partial v}{\partial x}\right). \tag{18}$$

The RHS of the above equation can also be expressed in terms of the stress σ and vorticity ω,

$$\Delta p = -\frac{1}{2}(\sigma^2 - \omega^2), \tag{19}$$

where $\sigma^2 = s_{11}^2 + s_{12}^2$ and $s_{11} = 2\partial_x u = -2\partial_y v$, $s_{12} = \partial_y u + \partial_x v$. Both s_{11} and s_{12} are components of the stress tensor. An alternative form of the PPE has been derived by

Salih in [20], where the RHS is written in terms of derivatives of the streamfunction only,

$$\Delta p = 2\left[\frac{\partial^2\psi}{\partial x^2}\frac{\partial^2\psi}{\partial y^2} - \left(\frac{\partial^2\psi}{\partial x \partial y}\right)^2\right]. \tag{20}$$

The above form of the PPE might be particularly useful in the context of solving the Vorticity Transport Equation, since it does not involve the velocity vector and, therefore, the pressure can be directly computed if the pair (ω, ψ) is known. All equations (18), (19) and (20) are defined inside the bounded domain Ω. We still need some relations that associate the pressure function with either the vorticity or streamfunction on the boundary $\partial\Omega$. There are different approaches to find suitable boundary conditions. One of them has been suggested by Salih in [20], where the author derives a couple of pressure-vorticity relations in Cartesian coordinate system. For the purpose of this project, we will correlate the vorticity and pressure in the normal/tangential coordinate system. A sketch of such a system is provided in Figure 1.

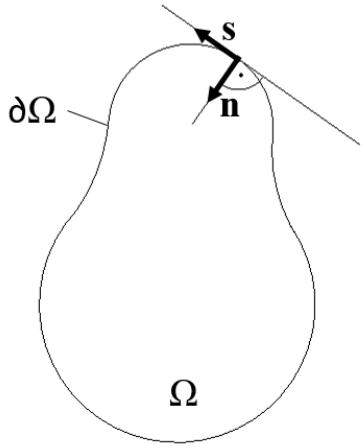

Figure 1: Normal and tangent vectors to the boundary $\partial\Omega$.

Using the definition of the vorticity and assuming no-slip boundary conditions, we can

re-express this quantity in the normal/tangiential system:

$$\omega = \left[-\frac{\partial}{\partial n}, \frac{\partial}{\partial s}\right] \cdot [v_s, v_n] = -\frac{\partial v_s}{\partial n}, \tag{21}$$

where v_s and v_n are respectively tangential and normal components of the velocity field $\mathbf{v}$. We can now project equation (1a) on the normal vector $\mathbf{n}$ and write the normal derivative of the pressure function as a function of the vorticity,

$$\begin{aligned}\frac{\partial p}{\partial n} = \nu \mathbf{n} \cdot \Delta \mathbf{v} = \nu \left(\frac{\partial^2}{\partial s^2} + \frac{\partial^2}{\partial n^2}\right) \mathbf{v}_n = \nu \frac{\partial}{\partial n}\frac{\partial v_n}{\partial n} = -\nu \frac{\partial}{\partial n}\frac{\partial v_\tau}{\partial s} \\ = \nu \frac{\partial}{\partial s}\left(-\frac{\partial v_\tau}{\partial n}\right) = \nu \frac{\partial \omega}{\partial s}.\end{aligned} \tag{22}$$

Analogously, making use of the same properties of the velocity field and the projection of (1a) on $\mathbf{s}$, one can derive the tangential derivative of the pressure function,

$$\frac{\partial p}{\partial s} = \nu \mathbf{s} \cdot \Delta \mathbf{v} = \nu \left(\frac{\partial^2}{\partial s^2} + \frac{\partial^2}{\partial n^2}\right) \mathbf{v}_\tau = \nu \frac{\partial}{\partial n}\frac{\partial v_\tau}{\partial n} = -\nu \frac{\partial \omega}{\partial n}. \tag{23}$$

These two identities, (22) and (23), are defined on the boundary $\partial\Omega$ and resemble the Cauchy-Riemann equations for complex-analytic functions, but the similarity is only superficial. We can now utilize them to close the Pressure Poisson Equation. Since they are derived from NSE, either of them can serve as a boundary condition for the PPE.

2.3 Instantaneous Growth of Enstrophy

Another aspect of the Navier-Stokes equation, relevant for this project, is the instantaneous rate of the enstrophy growth that is simply computed by taking the time derivative of $\mathcal{E}$,

$$\frac{\mathrm{d}\mathcal{E}}{\mathrm{d}t} = \frac{1}{2}\frac{\mathrm{d}}{\mathrm{d}t}\int_\Omega \omega^2 \mathrm{d}\Omega = \int_\Omega \omega \frac{\partial \omega}{\partial t}\mathrm{d}\Omega = -\int_\Omega \omega(\mathbf{v}\cdot\nabla)\omega \mathrm{d}\Omega + \nu \int_\Omega \omega \Delta \omega \mathrm{d}\Omega. \tag{24}$$

Furthermore, using the fact that the velocity is a divergence-free vector field, one can show that the cubic term of (24) vanishes. Since

$$\int_\Omega \omega(\mathbf{v}\cdot\nabla)\omega \mathrm{d}\Omega = \int_\Omega \omega\nabla\cdot(\omega\mathbf{v})\mathrm{d}\Omega = -\int_\Omega \omega(\mathbf{v}\cdot\nabla)\omega + \oint_{\partial\Omega}\omega^2(\mathbf{v}\cdot\mathbf{n})\mathrm{d}\sigma, \tag{25}$$

and due to the non-slip boundary conditions the line integral cancels out, which means that the cubic term also disappears. Thus, the instantaneous enstrophy growth can be written in the following form:

$$\boxed{\frac{\mathrm{d}\mathcal{E}}{\mathrm{d}t} = \nu\int_\Omega \omega\Delta\omega\mathrm{d}\Omega}. \tag{26}$$

This relation constitutes the central part of this thesis, since we are interested in computing the maximum value of $\mathrm{d}\mathcal{E}/\mathrm{d}t$ for a given value of the initial enstrophy $\mathcal{E}_0$. Unlike in the case of periodic domains, (26) is not sign-definite, since after the integration by parts,

$$\int_\Omega \omega\Delta\omega\mathrm{d}\Omega = -\int_\Omega |\nabla\omega|^2\mathrm{d}\Omega + \oint_{\partial\Omega}\frac{\partial\omega}{\partial n}\omega\mathrm{d}\sigma, \tag{27}$$

the boundary term does not vanish. The following chapters cover a detailed description of both mathematical and computational tools that will enable us to determine the maximum of $\mathrm{d}\mathcal{E}/\mathrm{d}t$ for given fields ω with prescribed enstrophy $\mathcal{E}_0$.

3 Maximum Enstrophy Growth as a Variational Optimization Problem

Our goal is to compute the maximum enstrophy growth for fields ω with a prescribed initial enstrophy $\mathcal{E}_0$. We will solve this optimization problem using basic tools of the optimization theory and calculus of variations. According to [12], there are four major elements of most optimization problems:

- An objective functional $\mathcal{J}$,
- Control variables and control space,
- State variables and state space,
- Any constraints imposed on both control and state variables.

As regards the objective (cost) functional, it is naturally defined as the time derivative of the enstrophy, thus

$$\mathcal{J}(\omega) = \frac{\mathrm{d}\mathcal{E}}{\mathrm{d}t} = \nu \int_{\Omega} \omega \Delta \omega \mathrm{d}\Omega. \tag{28}$$

The vorticity field ω such that $\mathcal{E}(\omega) = \mathcal{E}_0$ is our control variable. We can understand this quantity as the initial condition for the vorticity transport equation (12). Both the control and state spaces must be Sobolev spaces $H^1(\Omega)$. This is the minimum regularity requirement based on the trace theorem and will be explained in detail in the subsequent sections of this chapter. Since we consider a bounded domain, we have to take into account the constraint associated with the no-slip boundary conditions for the velocity field. Moreover, we also must ensure that the Pressure Poisson Equation

is satisfied. Using the streamfunction and vorticity as the state variables, however, we can incorporate these requirements into our optimization problem, which can formally be written in the following way:

$$\max_{\omega \in H^1(\Omega)} \mathcal{J}(\omega) \tag{29a}$$

$$\text{subject to} \qquad \frac{1}{2}\int_\Omega \omega^2 \mathrm{d}\Omega = \mathcal{E}_0, \tag{29b}$$

$$\Delta\psi = -\omega \qquad \text{in } \Omega, \tag{29c}$$

$$\Delta p = 2\left[\frac{\partial^2\psi}{\partial x^2}\frac{\partial^2\psi}{\partial y^2} - \left(\frac{\partial^2\psi}{\partial x \partial y}\right)^2\right] \qquad \text{in } \Omega, \tag{29d}$$

$$\psi = \frac{\partial\psi}{\partial n} = 0 \qquad \text{on } \partial\Omega. \tag{29e}$$

It is clear now that the presence of constraints (29b) and (29d) makes this problem nonlinear, meaning that we will need to apply a suitable iterative method. There exist few well-known methods of solving optimization problems of this class. For the purpose of this project, we will focus on, first, the Eulerian-Lagrangian formulation approach and, second, the gradient-based method. While the latter is more convenient from the numerical point of view, the Euler-Lagrange formulation is nonetheless very useful as it provides valuable insights about the structure of the optimization problem.

3.1 Euler-Lagrange Equations

Proposed in the mid-eighteenth century, the Euler-Lagrange equation is a very useful tool to characterize maxima (or minima) of functionals. The method of computing the extrema of a functional is analogous to the well-known Fermat's theorem (also known as interior extremum theorem), which says that a local extremum corresponds to the point at which the first derivative (perturbation) of a function vanishes. However, before we perturb functional (28), we have to incorporate the constraints listed in (29) by adding

extra terms and multiplying them by suitable Lagrange multipliers. Therefore, let us augment (28) in the following way,

$$\mathcal{J}_A(\omega) = \mathcal{J}(\omega) + \lambda\left(\frac{1}{2}\int_\Omega \omega^2 \mathrm{d}\Omega - \mathcal{E}_0\right) + \int_\Omega \varphi\left(\Delta\psi + \omega\right)\mathrm{d}\Omega, \tag{30}$$

where the constant λ and function $\varphi = \varphi(\mathbf{x})$ are the Lagrange multipliers. Subsequently, we can compute the perturbation of the augmented functional and set it to zero, i. e.

$$\mathcal{J}'_A(\omega, \omega') = \nu\int_\Omega \omega\Delta\omega' + \omega'\Delta\omega \mathrm{d}\Omega + \lambda\int_\Omega \omega\omega' \mathrm{d}\Omega + \int_\Omega \varphi(\Delta\psi' + \omega')\mathrm{d}\Omega = 0. \tag{31}$$

To construct a system of Euler-Lagrange equations, we have to expand (31) integrating it by parts,

$$\begin{aligned} J'_A(\omega, \omega') = 2\nu\int_\Omega \Delta\omega\omega' \mathrm{d}\Omega + \nu\oint_{\partial\Omega} \omega'\frac{\partial\omega}{\partial n} - \omega\frac{\partial\omega'}{\partial n}\mathrm{d}\sigma + \lambda\int_\Omega \omega\omega' \mathrm{d}\Omega \\ + \int_\Omega \Delta\varphi\psi' + \varphi\omega' \mathrm{d}\Omega + \oint_{\partial\Omega} \varphi\frac{\partial\psi'}{\partial n} - \psi'\frac{\partial\varphi}{\partial n}\mathrm{d}\sigma \\ = \int_\Omega (2\nu\Delta\omega + \lambda\omega + \varphi)\omega' \mathrm{d}\Omega + \int_\Omega \Delta\varphi\psi' \mathrm{d}\Omega - \nu\oint_{\partial\Omega} \omega'\frac{\partial\omega}{\partial n} + \omega\frac{\partial\omega'}{\partial n}\mathrm{d}\sigma = 0, \end{aligned} \tag{32}$$

and setting all terms proportional to ω' and ψ' to zero. We can observe that in the boundary integral of (32), there is a normal derivative of the perturbed vorticity, which prevents us from directly setting up the system of Euler-Lagrange equations. In order to overcome this obstacle, we will make use of boundary relation (23) between the vorticity and pressure that was derived in the previous chapter. Therefore, by performing integration by parts with respect to σ, the term in question in (32) can be rewritten as follows:

$$\nu\oint_{\partial\Omega} \omega\frac{\partial\omega'}{\partial n}\mathrm{d}\sigma = -\oint_{\partial\Omega} \omega\frac{\partial p'}{\partial s}\mathrm{d}\sigma = \oint_{\partial\Omega} \frac{\partial\omega}{\partial s}p'\mathrm{d}\sigma. \tag{33}$$

It is now evident that we need another relation between the (perturbed) pressure and vorticity in order to express the former. Putting (19) and (22) together and computing their perturbations with respect to ω', we end up with a Poisson PDE for p',

$$\Delta p' = -\sigma\sigma' + \omega\omega' \qquad \text{in } \Omega, \tag{34a}$$

$$\frac{\partial p'}{\partial n} = \nu \frac{\partial \omega'}{\partial s} \qquad \text{on } \partial\Omega. \tag{34b}$$

One can easily notice that the term $\sigma\sigma'$ is a function of the velocity, which should be further represented in terms of the vorticity,

$$\mathbf{v}(\mathbf{x}) = \int_\Omega \mathbf{K}(\mathbf{x}, \mathbf{x}')\omega(\mathbf{x}')\mathrm{d}\Omega + \nabla\phi, \tag{35}$$

where $\mathbf{K}$ denotes the Biot-Savart kernel defined as

$$\mathbf{K}(\mathbf{x}, \mathbf{x}') = \frac{1}{2\pi}\frac{(\mathbf{x} - \mathbf{x}')^\perp}{|\mathbf{x} - \mathbf{x}'|^2}, \tag{36}$$

while ϕ is the potential required to satisfy the wall-normal velocity boundary condition. It is the solution of the following Laplace's equation,

$$\Delta\phi = 0 \qquad \text{in } \Omega, \tag{37a}$$

$$\frac{\partial \phi}{\partial n} = -\mathbf{n} \cdot \int_\Omega \mathbf{K}(\mathbf{x}, \mathbf{x}')\omega(\mathbf{x}')\mathrm{d}\Omega \qquad \text{on } \partial\Omega. \tag{37b}$$

To shorten the notation, we can write ϕ as a function of the vorticity using the integral (convolution) operator $\mathcal{L}$ associated with sytem (37) as $\phi = \mathcal{L} * \omega$. Thanks to the linearity of systems (34) and (37), we define the perturbed pressure function on the boundary as

follows,

$$\begin{aligned} p'|_{\partial\Omega} = &\int_\Omega \mathbf{G}(\mathbf{x},\mathbf{x}'')\omega\omega'\mathrm{d}\Omega \\ &+ \int_\Omega \mathbf{G}(\mathbf{x},\mathbf{x}'')\Bigg\{4\frac{\partial u}{\partial x}\left[\int_\Omega \mathbf{D}_1\cdot\mathbf{K}(\mathbf{x}'',\mathbf{x}')\omega(\mathbf{x}')\mathrm{d}\Omega + \mathbf{D}_1\cdot\nabla\mathcal{L}*\omega'\right] \\ &+ \left(\frac{\partial u}{\partial y}+\frac{\partial v}{\partial x}\right)\left[\int_\Omega \mathbf{D}_2\cdot\mathbf{K}(\mathbf{x}'',\mathbf{x}')\omega(\mathbf{x}')\mathrm{d}\Omega + \mathbf{D}_2\cdot\nabla\mathcal{L}*\omega'\right]\Bigg\}\mathrm{d}\Omega \\ &+ \nu M\frac{\partial\omega'}{\partial s}, \end{aligned} \tag{38}$$

where $\mathbf{D}_1 = \left[\frac{\partial}{\partial x},0\right]^T$ and $\mathbf{D}_2 = \left[\frac{\partial}{\partial y},\frac{\partial}{\partial x}\right]^T$ denote differential operators, M is a Neumann-to-Dirichlet operator, while $\mathbf{G}$ denotes the fundamental solution of Laplace's equation in 2D space given by

$$\mathbf{G}(\mathbf{x},\mathbf{x}') = \frac{1}{2\pi}\ln|\mathbf{x}-\mathbf{x}'|. \tag{39}$$

Finally, we can plug (38) in (33) and derive the final form of the objective functional in which all terms will be proportional to either ω' or ψ',

$$\begin{aligned} \mathcal{J}'_A(\omega,\omega') = &\int_\Omega\Bigg\{\left[2\nu\Delta\omega+\lambda\omega+\varphi\right]\omega' + \omega\left[\oint_{\partial\Omega}\frac{\partial\omega}{\partial s}\mathbf{G}(\mathbf{x},\mathbf{x}')\mathrm{d}s\right] \\ &+ \oint_{\partial\Omega}\frac{\partial\omega}{\partial s}\int_\Omega \mathbf{G}(\mathbf{x},\mathbf{x}'')\Bigg[4\frac{\partial u}{\partial x}\left(\mathbf{D}_1\cdot\mathbf{K}(\mathbf{x}'',\mathbf{x}')+\mathbf{D}_1\cdot\nabla\mathcal{L}(\mathbf{x}'',\mathbf{x}')\right) \\ &+ \left(\frac{\partial u}{\partial y}+\frac{\partial v}{\partial x}\right)\left(\mathbf{D}_2\cdot\mathbf{K}(\mathbf{x}'',\mathbf{x}')+\mathbf{D}_2\cdot\nabla\mathcal{L}(\mathbf{x}'',\mathbf{x}')\right)\Bigg]\mathrm{d}\sigma\mathrm{d}\Omega\,\omega'\Bigg\}\mathrm{d}\Omega \\ &+ \int_\Omega \Delta\varphi\psi'\mathrm{d}\Omega + \nu\oint_{\partial\Omega}\left[\frac{\partial\omega}{\partial n}-\frac{\partial}{\partial s}M^*\frac{\partial\omega}{\partial s}\right]\omega'\mathrm{d}\sigma = 0, \end{aligned} \tag{40}$$

where M^* is the adjoint of the Neumann-to-Dirichlet map M. The final step is to convert (40) to the system of Euler-Lagrange equations simply by setting all the terms proportional to ω' and ψ' to zero, in compliance with the fundamentals of calculus of variations. Thus, including the initial enstrophy constraint, the full system can be

written in the following form:

$$
\begin{aligned}
&2\nu\Delta\omega + \lambda\omega + \varphi + \omega\left[\oint_{\partial\Omega}\frac{\partial\omega}{\partial s}\mathbf{G}(\mathbf{x},\mathbf{x}')\mathrm{d}s\right] \\
&+\oint_{\partial\Omega}\frac{\partial\omega}{\partial s}\int_{\Omega}\mathbf{G}(\mathbf{x},\mathbf{x}'')\left[4\frac{\partial u}{\partial x}\left(\mathbf{D}_1\cdot\mathbf{K}(\mathbf{x}'',\mathbf{x}')+\mathbf{D}_1\cdot\nabla\mathcal{L}(\mathbf{x}'',\mathbf{x}')\right)\right. \qquad \text{in } \Omega, \qquad (41a)\\
&\left.+\left(\frac{\partial u}{\partial y}+\frac{\partial v}{\partial x}\right)\left(\mathbf{D}_2\cdot\mathbf{K}(\mathbf{x}'',\mathbf{x}')+\mathbf{D}_2\cdot\nabla\mathcal{L}(\mathbf{x}'',\mathbf{x}')\right)\right]\mathrm{d}\sigma\mathrm{d}\Omega = 0 \\
&\Delta\psi = -\omega \qquad \text{in } \Omega, \qquad (41b)\\
&\Delta\varphi = 0 \qquad \text{in } \Omega, \qquad (41c)\\
&\psi = \frac{\partial\psi}{\partial n} = 0 \qquad \text{on } \partial\Omega, \qquad (41d)\\
&\frac{\partial\omega}{\partial n} = \frac{\partial}{\partial s}M^*\frac{\partial\omega}{\partial s} \qquad \text{on } \partial\Omega, \qquad (41e)\\
&\frac{1}{2}\int_{\Omega}\omega^2\mathrm{d}\Omega = \mathcal{E}_0 \quad \text{(enstrophy constraint).} \qquad (41f)
\end{aligned}
$$

The pair (ω, ψ) satisfying system (41) is the solution to optimization problem (29). We can see that the derived Euler-Lagrange system is nonlinear, which is evident in equations (41a) and (41f). It consists of three equations defined inside the domain Ω, each involving a Laplace operator. Additionally, the system includes three boundary conditions, two associated with the streamfunction and one with the vorticity. Although there are no explicit boundary conditions for φ, we conclude that the system is well-posed. From the numerical point of view, solving (41) directly might be very challenging, since one would have to set up a costly Newton's iteration scheme for a problem of the type $f(\mathbf{x}) = \mathbf{0}$, where $\mathbf{x}$ is a vector containing all the three unknown functions. Moreover, since the whole system has been constructed using the standard Euler-Lagrange formulation, it also involves Lagrange multipliers that would be somehow evaluated during Newton's iteration. Another numerical challenge is the accurate inversion of elliptic operators, using the Green's function or Biot-Savart kernel. To avoid these difficulties, one could

solve the maximization problem using a completely different approach, a method that is much more computationally-friendly, namely the gradient-based method.

3.2 Gradient-Based Method

Since the main goal of this work is to find the maximum instantaneous growth of enstrophy, i. e., to solve the optimization problem (29), we can apply a very convenient computational method belonging to the family of gradient-based methods for maximization problems. The idea is to utilize one of the popular optimization algorithms, such as the steepest ascent method. Regardless of the specific method choice, it is necessary to derive the gradient of the objective functional. This section highlights all mathematical tools we need to derive the gradient of $\mathcal{J}$ with respect to the H^1 topology, including the definition of the Gateaux differential and the Riesz representation theorem.

By the first-order optimality condition (31), we know that the perturbation of the augmented cost function is zero. In addition, according to the results presented by Luenberger [15], we can write the perturbation of the cost function in terms of the Gateaux (directional) derivative, i. e.

$$\mathcal{J}'(\omega, \omega') = \lim_{\epsilon \to 0} \frac{\mathcal{J}(\omega + \epsilon\omega') - \mathcal{J}(\omega)}{\epsilon}, \tag{42}$$

where ω' represents an arbitrary direction of the perturbation in the space $H^1(\Omega)$. According to (32), the above Gateaux differential can be rewritten as

$$\begin{aligned} \mathcal{J}'(\omega, \omega') &= \int_\Omega 2\nu \Delta\omega\omega' \mathrm{d}\Omega - \nu \oint_{\partial\Omega} \omega' \frac{\partial\omega}{\partial n} - \omega \frac{\partial\omega'}{\partial n} \mathrm{d}\sigma \\ &= \int_\Omega 2\nu \Delta\omega\omega' \mathrm{d}\Omega - \nu \oint_{\partial\Omega} \omega' \frac{\partial\omega}{\partial n} \mathrm{d}\sigma + \oint_{\partial\Omega} \frac{\partial\omega}{\partial s} p' \mathrm{d}s. \end{aligned} \tag{43}$$

The terms associated with the Lagrange multipliers of the perturbed augmented cost functional (32) can also be expressed in the analogous way, however, these terms are not critical in our algorithm. To find the vorticity field $\tilde{\omega}$ that maximizes cost functional (28), one can use the following iterative steepest-ascent method

$$\omega^{(n+1)} = \omega^{(n)} + \tau_n \nabla^{H^1} \mathcal{J}(\omega^{(n)}), \tag{44a}$$

$$\omega^{(0)} = \omega_*, \tag{44b}$$

where ω_* is the initial guess for the maximizing vorticity field such that the corresponding streamfunction satisfies two homogeneous boundary conditions, i. e. $\psi_* = \frac{\partial \psi_*}{\partial n} = 0$ and $\omega_* = -\Delta\psi_*$ and, moreover, both boundary vorticity-pressure relations (22)–(23) hold. Consequently, $\omega^{(n)}$ can be viewed as an approximation of $\tilde{\omega}$ after the nth iteration and $\tilde{\omega} = \lim_{n\to\infty} \omega^{(n)}$, while τ_n is the step size which may vary from iteration to iteration. One can notice that this approach does not involve the evaluation of the Lagrange multipliers, which would be inevitable using Newton's method to solve (41).

The central part of this algorithm is the evaluation of the cost functional gradient, $\nabla^{H^1}\mathcal{J}(\omega)$, in the H^1 topology. Before we derive it, however, it is very important to explain why the H^1 space is necessary for the vorticity function. Cost functional (28) can be integrated by parts giving rise to two integrals (see (27)), $\int_\Omega (\nabla\omega)^2 \mathrm{d}\Omega$ and $\oint_{\partial\Omega} \omega \frac{\partial\omega}{\partial n} \mathrm{d}\sigma$. The former indicates clearly that the regularity requirement is $\omega \in H^1$. An analogous analysis for the line integral is not so straightforward. Nevertheless, we can use the trace theorem [6] to verify that the space H^1 offers sufficient regularity for the vorticity on the boundary. Therefore if $\omega \in H^1(\Omega)$ and $\nabla\omega \in L_2(\Omega)$ in Ω, then, by the trace theorem, $\omega \in H^{1/2}(\partial\Omega)$ and $\nabla\omega \in H^{-1/2}(\partial\Omega)$. This observation leads to the conclusion that the line integral $\oint \omega \frac{\partial\omega}{\partial n} \mathrm{d}\sigma$ is bounded as long as $\omega \in H^1(\Omega)$. It means that the H^1 topology is sufficient for the objective functional and its Gateaux differential to be well defined.

We can now use the Riesz representation theorem [21] to find the relation between $\mathcal{J}'(\omega, \omega')$ and the gradient $\nabla^{H^1}\mathcal{J}(\omega)$. Before we utilize this theorem, we must define inner products in the L_2 and H^1 topologies, respectively,

$$\langle z_1, z_2 \rangle_{L_2} = \int_\Omega z_1 z_2 \mathrm{d}\Omega \qquad \forall z_1, z_2 \in L_2(\Omega), \tag{45a}$$

$$\langle z_1, z_2 \rangle_{H^1} = \int_\Omega z_1 z_2 \mathrm{d}\Omega + l \int \nabla z_1 \cdot \nabla z_2 \mathrm{d}\Omega \qquad \forall z_1, z_2 \in H^1(\Omega). \tag{45b}$$

The parameter l is an adjustable constant [19] and, in our derivations, is assumed to be 1. Therefore, as functional (28) is linear and bounded, the following identity is true,

$$\mathcal{J}'(\omega, \omega') = \left\langle \nabla^{L_2}\mathcal{J}(\omega), \omega' \right\rangle_{L_2} = \left\langle \nabla^{H^1}\mathcal{J}(\omega), \omega' \right\rangle_{H^1}. \tag{46}$$

Before we proceed, however, we will state and prove a lemma that is crucial not only in the anlysis of the L_2-gradient, but also throughout the entire thesis.

Lemma 1. *Let f be a sufficiently smooth harmonic function. If the vorticity function ω corresponds to a velocity field satisfying no-slip boundary conditions* (1c)*, then $\int_\Omega \omega f \mathrm{d}\Omega = 0$.*

Proof. Using Green's identities,

$$\int_\Omega \Delta\psi f - \Delta f \psi \mathrm{d}\Omega = \oint_{\partial\Omega} \frac{\partial \psi}{\partial n} f - \frac{\partial f}{\partial n}\psi \mathrm{d}\sigma \tag{47}$$

and relations (15), (16), we conclude that

$$\int_\Omega \omega f \mathrm{d}\Omega = 0. \tag{48}$$

□

Thus, in the L_2 topology, the gradient $\nabla^{L_2}\mathcal{J}(\omega)$ is defined up to a harmonic function, which means that for every function f such that $\Delta f = 0$, the identity

$$\left\langle \nabla^{L_2}\mathcal{J}(\omega), \omega' \right\rangle_{L_2} = \left\langle \nabla^{L_2}\mathcal{J}(\omega) + f, \omega' \right\rangle_{L_2} \tag{49}$$

always holds. Similarly, for any constant $c \in \mathbb{R}$, we have the following identity for the H^1 inner products and associated gradients,

$$\left\langle \nabla^{H^1}\mathcal{J}(\omega), \omega' \right\rangle_{H^1} = \left\langle \nabla^{H^1}\mathcal{J}(\omega) + c, \omega' \right\rangle_{H^1}, \tag{50}$$

which is true because the vorticity has zero mean. Applying the definition of the H^1 inner product, we will rewrite identity (46) explicitly and then integrate it by parts in order obtain a form that is consistent with (43),

$$\begin{aligned} \mathcal{J}'(\omega, \omega') = \left\langle \nabla^{H^1}\mathcal{J}(\omega), \omega' \right\rangle_{H^1} &= \int_\Omega \left(\nabla^{H^1}\mathcal{J}(\omega)\right)\omega' + \nabla\left(\nabla^{H^1}\mathcal{J}(\omega)\right)\cdot\nabla\omega' \mathrm{d}\Omega \\ &= \int_\Omega \left[(\mathrm{Id} - \Delta)\,\nabla^{H^1}\mathcal{J}(\omega)\right]\omega' \mathrm{d}\Omega + \oint_{\partial\Omega} \frac{\partial}{\partial n}\left[\nabla^{H^1}\mathcal{J}(\omega)\right]\omega' \mathrm{d}\sigma. \end{aligned} \tag{51}$$

The ultimate goal of further steps is to re-express (51) in a way that both the area and boundary integrals involve functions that explicitly involve ω' as a factor which will allow us to involve the Riesz theorem. This formula satisfies our needs except for the boundary integral involving the perturbation of the pressure field p'. In order to rewrite this term to a more convenient form, we will make use of the harmonic function f satisfying

$$\Delta f = 0 \qquad \text{in } \Omega, \tag{52a}$$

$$\frac{\partial f}{\partial n} = \frac{\partial \omega}{\partial s} \qquad \text{on } \partial\Omega. \tag{52b}$$

Moreover, we will consider elliptic system (34), thanks to which the pressure perturbation can be expressed in terms both the perturbed velocity and vorticity fields. By linearity, the solution to this system can be represented as a superposition of solutions p_1 and p_2 to two subproblems,

$$\Delta p_1' = 0 \qquad \text{in } \Omega, \tag{53a}$$

$$\frac{\partial p_1'}{\partial n} = \nu \frac{\partial w'}{\partial s} \qquad \text{on } \partial\Omega, \tag{53b}$$

and

$$\Delta p_2' = 2\left(\frac{\partial u'}{\partial x}\frac{\partial v}{\partial y} + \frac{\partial u}{\partial x}\frac{\partial v'}{\partial y} - \frac{\partial u'}{\partial y}\frac{\partial v}{\partial x} - \frac{\partial u}{\partial y}\frac{\partial v'}{\partial x}\right) := R' \qquad \text{in } \Omega, \tag{54a}$$

$$\frac{\partial p_2'}{\partial n} = 0 \qquad \text{on } \partial\Omega. \tag{54b}$$

Using Green's identities, the relation

$$\oint_{\partial\Omega} \frac{\partial f}{\partial n} p_1' - \frac{\partial p_1'}{\partial n} f \mathrm{d}\sigma = \int_{\partial\Omega} p_1' \Delta f - f \Delta p_1' \mathrm{d}\Omega = 0 \tag{55}$$

is always true and, therefore, we have

$$\oint_{\partial\Omega} \frac{\partial \omega}{\partial s} p_1' \mathrm{d}\sigma = \oint_{\partial\Omega} \frac{\partial p_1'}{\partial n} f \mathrm{d}\sigma = \oint_{\partial\omega} \nu \frac{\partial \omega'}{\partial s} f \mathrm{d}\sigma = -\oint_{\partial\Omega} \nu \frac{\partial f}{\partial s} \omega' \mathrm{d}\sigma. \tag{56}$$

By the same token, we conclude that

$$\oint_{\partial\Omega} \frac{\partial \omega}{\partial s} p_2' \mathrm{d}\sigma = \int_{\Omega} p_2' \Delta f - f \Delta p_2' \mathrm{d}\Omega = -\int_{\Omega} f R' \mathrm{d}\Omega. \tag{57}$$

Combining the results from (56) and (57), we obtain a new form of the Gateaux differ-

ential,

$$\mathcal{J}'(\omega,\omega') = 2\nu\int_\Omega \omega'\Delta\omega \mathrm{d}\Omega - \int_\Omega fR'\mathrm{d}\Omega - \nu\oint_{\partial\Omega}\left(\frac{\partial f}{\partial s}+\frac{\partial\omega}{\partial n}\right)\omega'\mathrm{d}\sigma, \tag{58}$$

which is still not in a form consistent with Riesz theorem (46), since the integral $\int_\Omega fR'\mathrm{d}\Omega$ requires further treatment. Based on the fact that we impose two boundary conditions on the streamfunction ($\psi = \frac{\partial\psi}{\partial n} = 0$ on $\partial\Omega$), we infer that for every function h with sufficient regularity, the identity

$$\int_\Omega -\omega' h\mathrm{d}\Omega = \int_\Omega \psi'\Delta h\mathrm{d}\Omega \tag{59}$$

is always true, regardless of the boundary conditions satisfied by h (see Lemma 1). Subsequently, assuming that $\Delta h = \frac{\partial a}{\partial y}$ and denoting $a = \frac{\partial b}{\partial x}$, we conclude

$$-\int_\Omega \omega' h\mathrm{d}\Omega = \int_\Omega \Delta h\psi'\mathrm{d}\Omega = -\int_\Omega au'\mathrm{d}\Omega = \int_\Omega b\frac{\partial u'}{\partial x}\mathrm{d}\Omega, \tag{60}$$

where both a and b are smooth functions. Identity (60) clearly shows that the second integral of (58), consisting of derivatives of the velocity vector components, can be rewritten to a form, in which the integrand is proportional to ω'. Making use of this observation, we can now define a new function g that satisfies

$$\begin{aligned}\Delta g = 2\Bigg(&\frac{\partial^2}{\partial x\partial y}\left(f\frac{\partial v}{\partial y}\right)+\frac{\partial^2}{\partial x^2}\left(f\frac{\partial u}{\partial y}\right)\\ &-\frac{\partial^2}{\partial x\partial y}\left(f\frac{\partial u}{\partial x}\right)-\frac{\partial^2}{\partial y^2}\left(f\frac{\partial v}{\partial x}\right)\Bigg) \qquad \text{in } \Omega, \end{aligned}\tag{61a}$$

$$g = \text{arbitrary} \qquad \text{on } \partial\Omega, \tag{61b}$$

which can be incorporared into (58) giving rise to the final form of the perturbed cost

functional (Gateaux differential),

$$\mathcal{J}'(\omega,\omega') = \int_\Omega \left[2\nu\Delta\omega + g\right]\omega' \mathrm{d}\Omega - \nu \oint_{\partial\Omega} \left[\frac{\partial f}{\partial s} + \frac{\partial \omega}{\partial n}\right]\omega' \mathrm{d}\sigma, \tag{62}$$

in which every term is proportional to ω', which means that our primary goal has been accomplished. The function g is a solution to a Poisson equations with *arbitrary* boundary condition, which is consistent with the fact that the L_2 gradient, $\nabla^{L_2}\mathcal{J}(\omega)$, is not unique and defined up to an arbitrary harmonic function. In the final step, we will make a comparison of (51) and (62), from which we can deduce the elliptic PDE system,

$$(\mathrm{Id} - \Delta)\,\nabla^{H^1}\mathcal{J}(w) = 2\nu\Delta\omega + g \qquad \text{in } \Omega, \tag{63a}$$

$$\frac{\partial}{\partial n}\left[\nabla^{H^1}\mathcal{J}(w)\right] = -\nu\left(\frac{\partial f}{\partial s} + \frac{\partial \omega}{\partial n}\right) \qquad \text{on } \partial\Omega, \tag{63b}$$

that enables us to compute the H^1 gradient. We observe that a Neumann boundary condition is imposed on $\nabla^{H^1}\mathcal{J}(w)$, and it may appear that the gradient is defined up to a constant. However, since the zero-mean property also applies to it, the H^1 gradient is indeed unique. In actual computations, one has to take this aspect into account by computing the appropriate constant when solving Neumann problem (63).

3.3 Solution in the Limit of Small Enstrophies $\mathcal{E}_0 \to 0$

It is possible to compute the solution of Euler-Lagrange system (41) in the limit $\mathcal{E}_0 \to 0$ by performing a formal series expansion in powers of the initial enstrophy $\mathcal{E}_0$, according to the analogous study that has been carried out by Ayala and Protas in [1]. This goal can be achieved in three main steps: first, a simpler form of (41) should be derived, using the previously defined functions f and g, second, all unknown functions are expanded

using a formal series expansion with respect to $\mathcal{E}_0$ and, finally, all the expansions should be plugged into the Euler-Lagrange equations, giving rise to a hierarchy of linear systems, each corresponding to a different power of $\mathcal{E}_0$. Making use of Gateaux differential (62) augmented by a term involving the initial enstrophy constraint (vide (31)),

$$\mathcal{J}'(\omega,\omega') = \int_\Omega \left[2\nu\Delta\omega + g\right]\omega' \mathrm{d}\Omega - \nu \oint_{\partial\Omega} \left[\frac{\partial f}{\partial s} + \frac{\partial \omega}{\partial n}\right]\omega' \mathrm{d}\sigma + \lambda \int_\Omega \omega\omega' \mathrm{d}\Omega, \tag{64}$$

and the functions f and g, we can write an Euler-Lagrange system, equivalent to (41), in the following way,

$$2\nu\Delta\omega + g = -\lambda\omega \qquad \text{in } \Omega, \tag{65a}$$

$$\Delta\psi + \omega = 0 \qquad \text{in } \Omega, \tag{65b}$$

$$\Delta f = 0 \qquad \text{in } \Omega, \tag{65c}$$

$$\Delta g - \mathcal{N}(\psi, f) = 0 \qquad \text{in } \Omega, \tag{65d}$$

$$\psi = \frac{\partial \psi}{\partial n} = 0 \qquad \text{on } \partial\Omega, \tag{65e}$$

$$\frac{\partial \omega}{\partial n} + \frac{\partial f}{\partial s} = 0 \qquad \text{on } \partial\Omega, \tag{65f}$$

$$\frac{\partial \omega}{\partial s} - \frac{\partial f}{\partial n} = 0 \qquad \text{on } \partial\Omega, \tag{65g}$$

$$\frac{1}{2}\int_\Omega \omega^2 \mathrm{d}\Omega = \mathcal{E}_0 \quad \text{(enstrophy constraint)}. \tag{65h}$$

where $\mathcal{N}(\omega)$ is a nonlinear term that corresponds to the RHS of (61) and is defined as

$$\begin{aligned}\mathcal{N}(\psi, f) = 2\Bigg(&\frac{\partial^2}{\partial x \partial y}\left(f\frac{\partial v}{\partial y}(\psi)\right) + \frac{\partial^2}{\partial x^2}\left(f\frac{\partial u}{\partial y}(\psi)\right) \\ &- \frac{\partial^2}{\partial x \partial y}\left(f\frac{\partial u}{\partial x}(\psi)\right) - \frac{\partial^2}{\partial y^2}\left(f\frac{\partial v}{\partial x}(\psi)\right)\Bigg).\end{aligned} \tag{66}$$

In order to examine the behaviour of the eigenpair $[(\omega, \psi, f, g)^T, \lambda]$ of Euler-Lagrange system (65) in the limit of $\mathcal{E}_0 \to 0$, we will use the following series expansions,

$$\omega = \omega_0 + \mathcal{E}_0^{1/2}\omega_1 + \mathcal{E}_0^1\omega_2 + \mathcal{O}(\mathcal{E}_0^{3/2}), \tag{67a}$$

$$\psi = \psi_0 + \mathcal{E}_0^{1/2}\psi_1 + \mathcal{E}_0^1\psi_2 + \mathcal{O}(\mathcal{E}_0^{3/2}), \tag{67b}$$

$$f = f_0 + \mathcal{E}_0^{1/2}f_1 + \mathcal{E}_0^1 f_2 + \mathcal{O}(\mathcal{E}_0^{3/2}), \tag{67c}$$

$$g = g_0 + \mathcal{E}_0^{1/2}g_1 + \mathcal{E}_0^1 g_2 + \mathcal{O}(\mathcal{E}_0^{3/2}), \tag{67d}$$

$$\lambda = \lambda_0 + \mathcal{E}_0^{1/2}\lambda_1 + \mathcal{E}_0^1\lambda_2 + \mathcal{O}(\mathcal{E}_0^{3/2}). \tag{67e}$$

In the next step we plug ansatz (67) into system (65), and collecting all terms proportional to $\mathcal{E}_0^0$, we obtain

$$2\nu\Delta\omega_0 + g_0 = -\lambda_0\omega_0 \qquad \text{in } \Omega, \tag{68a}$$

$$\Delta\psi_0 + \omega_0 = 0 \qquad \text{in } \Omega, \tag{68b}$$

$$\Delta f_0 = 0 \qquad \text{in } \Omega, \tag{68c}$$

$$\Delta g_0 - \mathcal{N}(\psi_0, f_0) = 0 \qquad \text{in } \Omega, \tag{68d}$$

$$\psi_0 = \frac{\partial\psi_0}{\partial n} = 0 \qquad \text{on } \partial\Omega, \tag{68e}$$

$$\frac{\partial\omega_0}{\partial n} + \frac{\partial f_0}{\partial s} = 0 \qquad \text{on } \partial\Omega, \tag{68f}$$

$$\frac{\partial\omega_0}{\partial s} - \frac{\partial f_0}{\partial n} = 0 \qquad \text{on } \partial\Omega, \tag{68g}$$

$$\frac{1}{2}\int_\Omega \omega_0^2 \mathrm{d}\Omega = 0 \quad \text{(enstrophy constraint)}, \tag{68h}$$

which implies that $\omega_0 \equiv 0$ and, consequently, the functions ψ_0, g_0 also vanish, while $f_0 = c_0$ is constant. Based on this conclusion, and the fact that

$$\mathcal{N}(\cdot, c_0) = 0, \tag{69}$$

we collect terms proportional to $\mathcal{E}_0^{1/2}$ giving rise to the linear system

$$-2\nu\Delta\omega_1 - g_1 = \lambda_0\omega_1 \qquad \text{in } \Omega, \tag{70a}$$

$$-\Delta\psi_1 - \omega_1 = 0 \qquad \text{in } \Omega, \tag{70b}$$

$$-\Delta f_1 = 0 \qquad \text{in } \Omega, \tag{70c}$$

$$-\Delta g_1 = 0 \qquad \text{in } \Omega, \tag{70d}$$

$$\psi_1 = \frac{\partial\psi_1}{\partial n} = 0 \qquad \text{on } \partial\Omega, \tag{70e}$$

$$\frac{\partial\omega_1}{\partial n} + \frac{\partial f_1}{\partial s} = 0 \qquad \text{on } \partial\Omega, \tag{70f}$$

$$\frac{\partial\omega_1}{\partial s} - \frac{\partial f_1}{\partial n} = 0 \qquad \text{on } \partial\Omega, \tag{70g}$$

$$\frac{1}{2}\int_\Omega \omega_1^2 \mathrm{d}\Omega = 1 \quad \text{(enstrophy constraint)}, \tag{70h}$$

which is in fact a generalized eigenvalue problem. Since we aim to obtain the solution in the limit $\mathcal{E}_0 \to 0$, it is sufficient to truncate all expansions at the order $\mathcal{O}(\mathcal{E}_0^1)$.
There are three important features of (70) that can be used in our further work. First and foremost, it provides a solution to the problem of the maximum enstrophy growth in the limit $\mathcal{E}_0 \to 0$. Second, the family of eigenfunctions ω_1 can be used in the steepest-ascent algorithm as the initial guess ω_*. Finally, it is relatively easy to implement the system, since it involves basic differential operators and, moreover, the unknown constant c_0 does no longer appear. In Appendix A, we investigate algebraic properties of eigenvalue problem (70) and, based on this analysis, we conclude that the eigenvalue λ_0 is indeed real, while the system is sign-definite. This fact is crucial, especially from the computational point of view, since one may encounter numerical problems in the case of square domains. Using the Chebyshev spectral method to discretize the LHS of system (70) we observe that the resulting matrix is singular, and therefore one needs additional treatment to desingularize it. A detailed description of numerical difficulties

associated with PDE operators of this type and possible remedies are included in the next chapter.

4 Numerical Methods

In this chapter we are going to review all numerical approaches that have been used to solve the optimization problem. Firstly, we will briefly review the Chebyshev spectral method, a spectral technique that is suitable for non-periodic domains. In the context of circular domains, we will also mention a hybrid Chebyshev-Fourier method. Moreover, a detailed description of computational problems associated with numerical implementation of eigenvalue problem (70) will be provided. Finally, we will highlight the most important aspects of the optimization algorithm and propose suitable methods to reduce the computational cost of the entire process.

4.1 Spectral Collocation Method

There exist two major families of fast spectral methods, the Fourier and Chebyshev method. The former is appropriate for periodic domains but, due to the Gibbs phenomenon at the boundaries, is not suitable for bounded domains. The latter, on the other hand, is free from this numerical artifact and therefore we are going to utilize it to discretize our unknown functions in space. Thus, every unknown function of a single variable, here denoted as $u(x)$, will be approximated using the discrete truncated Chebyshev series,

$$u(x) \approx u_N(x_i) = \sum_{k=0}^{N} \hat{u}_k T_k(x_i), \qquad i = 0, ..., N, \tag{71}$$

where x_i is a set of N collocation (interpolation) points, which in our case are the Gauss-Lobatto points defined by

$$x_i = \cos\left(\frac{\pi i}{k}\right), \qquad i = 0, ..., k, \tag{72}$$

while T_k denotes the Chebyshev polynomial of degree k defined for $x \in [-1, 1]$ as

$$T_k(x) = \cos(k\cos^{-1}x), \qquad k = 0, 1, 2, ... \tag{73}$$

Based on the Chebyshev approximation, we can easily differentiate any smooth function in the physical space. Assuming that $\mathbf{u}$ denotes an array of the values of $u(x_i)$ at N collocation points, the derivative $\mathbf{u}'$ can be easily computed as

$$\mathbf{u}' = \mathbf{D}_N\mathbf{u}, \tag{74}$$

where $\mathbf{u}'$ is a vector consisting of approximated values of $u'(x_i)$, while $\mathbf{D}_N$ denotes the Chebyshev differentiation matrix, whose detailed description can be found in [11]. The derivatives $\mathbf{u}^{(n)}$ of a higher order $n \geq 1$ can be obtained by elevating $\mathbf{D}_N$ to the power of n and applying the resulting matrix to $\mathbf{u}$. These recipes can be generalized to any higher space dimension. The present problem concerns two-dimensional domains and, therefore, we take a closer look at the approximation of functions of two variables and their derivatives. In the Cartesian coordinate system, we set up a grid based on N Gauss-Lobatto points in each direction, usually referred to as a "tensor-product grid". An example of the Cartesian grid of this type is illustrated in Figure 2(a). The most straightforward way to compute a partial derivative of the function $v(x, y)$ is to apply Kronecker products, according to [13]. Let $\mathbf{v}$ be the corresponding vector of function values, while $\mathbf{v}_x$ and $\mathbf{v}_y$ be arrays consisting of first-order partial derivatives of $\mathbf{v}$ w.r.t

the x- and y-coordinate, evaluated at the tensor product grid, then

$$\mathbf{v}_x = \mathbf{D}_N \otimes \mathbf{I}_N, \qquad \mathbf{v}_y = \mathbf{I}_N \otimes \mathbf{D}_N, \tag{75}$$

where $\mathbf{I}_N$ is an N-dimensional identity matrix, and the symbol $\otimes$ denotes the Kronecker product.

To discretize efficiently an equation or system of equations defined on a circular domain, one should transform the Cartesian coordinate system into the polar one using the following formulae:

$$x = r\cos\theta, \qquad y = r\sin\theta. \tag{76}$$

The most natural way to discretize a two-dimensional disk is to create a periodic Fourier (equispaced) grid in the azimuthal direction θ and a nonperiodic Chebyshev/Gauss-Lobatto grid in the radial direction r, such that

$$\theta \in [0, 2\pi], \qquad r \in [0, 1]. \tag{77}$$

Analogously to the 2D Cartesian case, we aim to construct a tensor-product grid, but this time each coordinate corresponds to a different node configuration. This also implies that the function $v(r, \theta)$ is approximated using the truncated Fourier series with respect to the azimuthal coordinate. Nonetheless, according to [22],the discretization of a circular domain, like the one above, exhibits some crucial drawbacks. One of them is unnecessary concentration of grid nodes near the origin $r = 0$, especially in the cases for which we expect smooth solutions. This approach is both inelegant and wasteful in terms of storage requirements. An interesting remedy for this inconvenience has been proposed by Fornberg in [9] and [10], who suggested to take $r \in [-1, 1]$ instead of $r \in [0, 1]$, while θ continues to span over $[0, 2\pi]$. The main characteristic of this representation is the

fact that each point (x, y) corresponds to two distinct points (r, θ). In other words, the map from (r, θ) to (x, y) is 2-to-1. Apart from the less severe point clustering near the origin, Fornberg's method features a reduced total number of gridpoints and, what is important, higher-order accuracy in the radial direction. Figure 2(b) shows a typical spectral grid based on the Chebshev-Fourier discretization. Another crucial aspect is that the Fourier pseudospectral method can still be applied in the azimuthal direction. From the practical point of view, it is important to notice a symmetry condition in (r, θ)-space:

$$v(r, \theta) = v(-r, (\theta + \pi) \mathrm{mod}\, 2\pi), \tag{78}$$

based on which it is relatively simple to assemble the differentiation matrix with respect to both polar coordinates, following the guidelines suggested by Trefethen in [22].

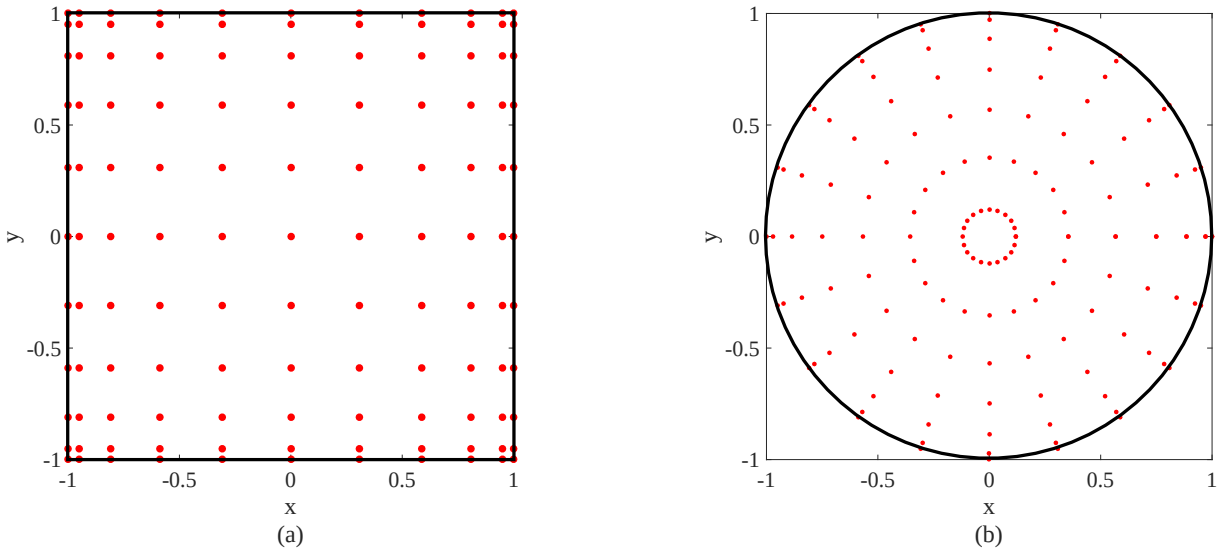

Figure 2: Spectral grids (red dots) based on Chebyshev discretization in the Cartesian coordinate system (a), and based on Chebyshev-Fourier discretization in the polar system (b).

A common disadvantage of spectral collocation methods is the fact that the differentiation matrix $\mathbf{D}_N$ is always poorly conditioned. This characteristic may play a crucial

role in solving large linear systems that are generated using such methods. On the other hand, however, both Chebyshev and Fourier methods, or a combination of both, guarantee spectral accuracy, provided the solution is analytic. In the case of standard finite-difference or finite-element methods, we observe algebraic convergence, which implies that for some constant $m > 0$ the error decreases as $\mathcal{O}(N^{-m})$ when $N \to \infty$. The spectral accuracy means that much faster convergence is achieved, namely $\mathcal{O}(c^{-N})$, where c is some positive constant. Figure 3 shows the convergence of the error in the numerical solution of a 2D Poisson equation with the source term and Dirichlet boundary conditions chosen such that the exact solution of the problem is $\mathrm{v}(x, y) = \mathrm{e}^{2(x+y)}$. The error is computed as an L_∞-norm of the difference between the numerical result $\mathrm{v}_N(x, y)$ and the manufactured analytical solution.

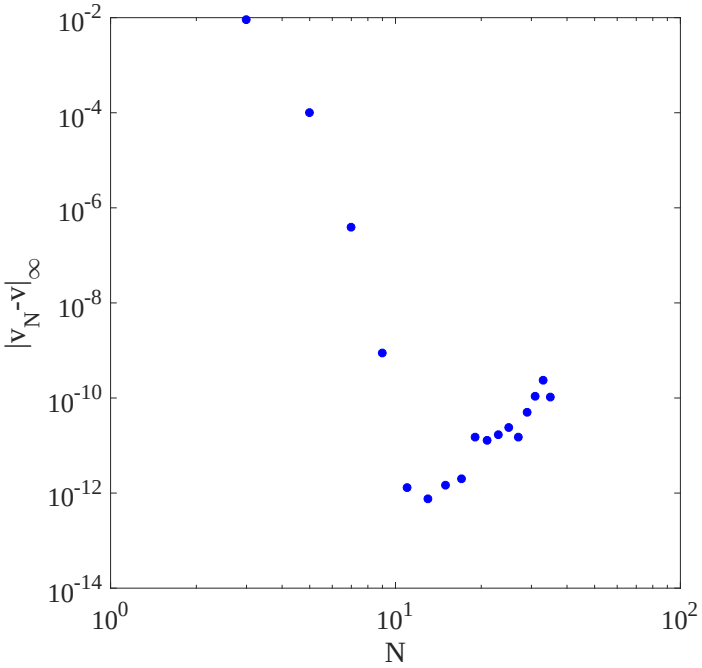

Figure 3: Relation between the absolute error and the grid resolution N in the solution of the test problem based on the 2D Poisson equation. This plot illustrates the accuracy of the Chebyshev spectral method.

We can observe that the error plot consists of two distinct branches. The first one, located in the left-hand side of the plot, clearly exhibits spectral convergence, that is, the error decreases with the rate of $\mathcal{O}(c^{-N})$. For $N > 10$, however, the error increases, which is a consequence of dominating round-off errors. This observation, however, does not imply that $N = 10$ is sufficient grid resolution for our main problem, which will be evident in Chapter 5.

4.2 Generalized Eigenvalue Problem

In this section, we will focus on a few numerical aspects involving solutions of the generalized eigenvalue problem (70), putting emphasis on the square domain. A few remarks regarding the circular domain, however, will be provided at the and of the section. Assuming a square domain $\Omega = [-1, 1] \times [-1, 1]$, all differential operators of this system are discretized using a Chebyshev spectral collocation method described as discussed in section 4.1. Consequently, the continuous linear system (70) is transformed to a generalized algebraic eigenvalue problem, which can be symbolically written as

$$\mathbf{A}\mathbf{y} = \lambda\mathbf{B}\mathbf{y}, \tag{79}$$

where $\mathbf{y}$ denotes a column vector with the discretizations of all four eigenfunctions stacked up in it. The matrix $\mathbf{A}$ corresponds to the PDE operator involving boundary conditions (LHS of the continuous sytem (70)), while $\mathbf{B}$ mostly consists of zeros, with the exception of rows associated with ω. Figure 4 illustrates the sparsity pattern of the matrices $\mathbf{A}$ and $\mathbf{B}$.

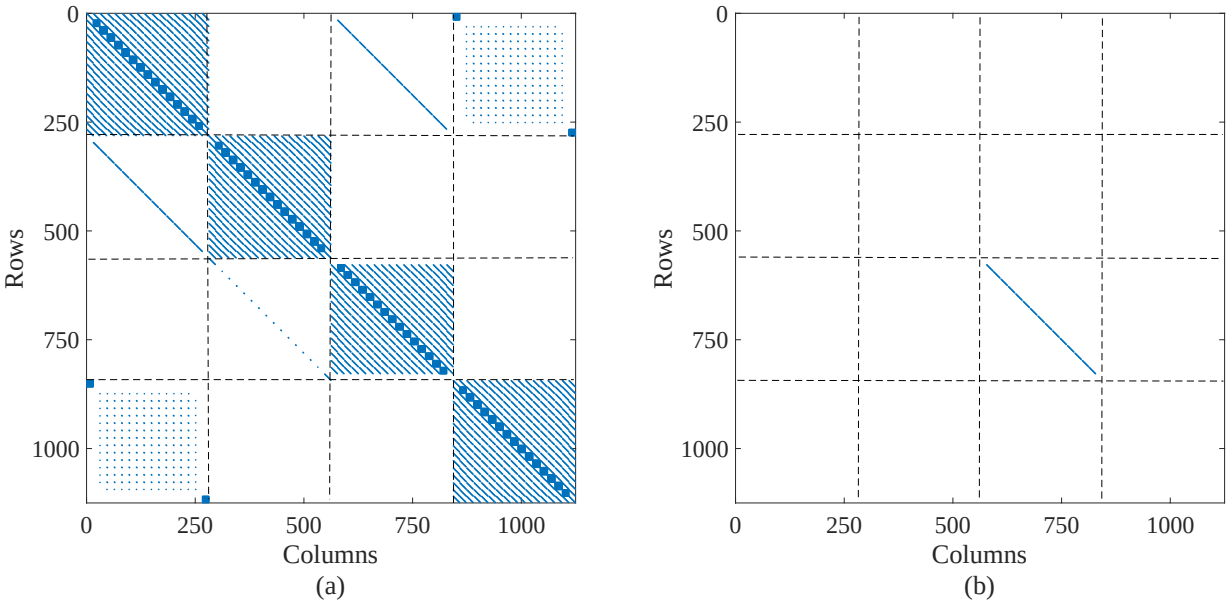

Figure 4: Sparsity patterns of the two block matrices, **A** (a) and **B** (b), generated for the resolution parameter $N = 16$ on the square domain. The dashed lines separate different blocks.

A careful inspection of the structure of the nature of **A** leads to the observation that it contains four zero columns, that correspond to the corner points of the $\tilde{g}_1$ function, therefore one needs to remove all the corner collocation points. In addition to that, a direct implementation of linear system (70) applying the Chebyshev collocation method leads to some other numerical difficulties. It turns out that, after the removal of all the corner nodes, the matrix **A** still features a total rank deficiency of 5. This problem has two different sources. First, due to the lack of Dirichlet boundary conditions, we observe that the function f_1 is defined up to a constant. Second, system (70) involves both a function ($\tilde{g}$) that has no prescribed boundary conditions and the streamfunction (ψ), on which homogeneous Dirichlet and Neumann boundary conditions are imposed. One can observe a very similar set of functions and boundary conditions in the Stokes system. As shown in [5], such a configuration results in numerical artifacts, which leads to four

null eigenvalues of (79). Therefore, in order to solve eigenvalue problem (79), we need to ensure that the rank of the matrix $\mathbf{A}$ is equal to its dimension. The first source can be neutralized easily by fixing the value of the f_1 function at an arbitrary node. The other problem, however, requires more sophisticated treatment. According to the extensive analysis of a very similar phenomenon presented by Peyret in his book [18], and also in [5] together with Ehrenstein, one has to remove another four collocation points. The choice of these four points is not obvious and must follow the rules introduced by Bwemba and Pasquetti in [4]. Ehrenstein and Peyret in [5] suggest to delete the following set of points:

$$P_1 = (x_1, -1), \quad P_2 = (x_{N-1}, -1), \quad P_3 = (x_1, 1), \quad P_4 = (x_{N-1}, 1).$$

Once all collocation points (both the corner points and the ones suggested above) are removed, the determinant of $\mathbf{A}$ is no longer zero. Thus, the generalized eigenvalue problem can be easily solved with any linear algebra package, for example, the command `[y,lambda]=eig(A,B)` in MATLAB solves (79) using the QZ algorithm. Due to a very large condition number of $\mathbf{A}$, the application of some high precision toolboxes might be inevitable [17].

In the case of a circular domain, no additional treatment is required. A direct implementation of the block matrices $\mathbf{A}$ and $\mathbf{B}$ leads a very similar structure as shown in Figure 4.

4.3 Optimization Algorithm

Finally, we will focus on the core part of the thesis, namely the optimization algorithm that was outlined in (44). To initiate the steepest ascent procedure for a given initial enstrophy $\mathcal{E}_0$, we need to determine three ingredients:

- the initial guess of the vorticity field ω_0,

- H^1 gradient $\nabla^{H^1}\mathcal{J}(\omega^n)$,
- step size τ_n.

Since the primary goal of this project is to find the maximum instantaneous enstrophy growth $\mathrm{d}\mathcal{E}/\mathrm{d}t$ for increasing enstrophy values $\mathcal{E}_0$, it is natural to use an eigenfunction of the eigenvalue problem (70) as the initial guess ω_*, since it provides the solution to the optimization problem in the limit $\mathcal{E}_0 \to 0$. The H^1 gradient can be easily computed by solving elliptic systems (52), (61) and (63) and, clearly, it must be updated at each iteration step. The step size τ_n can be evaluated in a variety of ways. An accurate computation of this parameter, however, might significantly accelerate the whole procedure and, therefore, the implementation of an efficient method might be inevitable. In this project we will use Brent's algorithm [3], where the evaluation of the step size

$$\tau_n = \arg\max_{\tau>0} \mathcal{J}(\omega^n + \tau\nabla^{H^1}\mathcal{J}(\omega^n)), \tag{80}$$

is based on an iterative procedure, whose task is to find the extremum of the function $\omega^n + \tau\nabla^{H^1}\mathcal{J}(\omega^n)$ by sampling it at a set of sample points. The MATLAB command `fminbnd()` utilizes exactly the same idea to find a minimum (or maximum) of a single-variable function.

Another important aspect of the optimization algorithm is a proper enforcement of the initial enstrophy constraint. In other words, we have to ensure that the L_2 norm of the vorticity field throughout the steepest ascent procedure is fixed and equal to $\mathcal{E}_0$. To satisfy this requirement, at every iteration step of both the steepest ascent and Brent's procedures the updated vorticity field $\omega^{n+1} = \omega^n + \tau\nabla^{H^1}\mathcal{J}(\omega^n)$ must be projected onto the set $\mathcal{V} = \{\omega \in H^1 : ||\omega||_{L_2} = 2\mathcal{E}_0\}$ by normalizing ω^{n+1} in the following way:

$$\omega^{n+1} := \frac{\omega^{n+1}}{||\omega^{n+1}||_{L_2}}\mathcal{E}_0. \tag{81}$$

The combination of line maximization (80) with constraint (81) can be interpreted as an arc optimization of the vorticity field ω over the set $\mathcal{V}$, which is schematically illustrated in Figure 5.

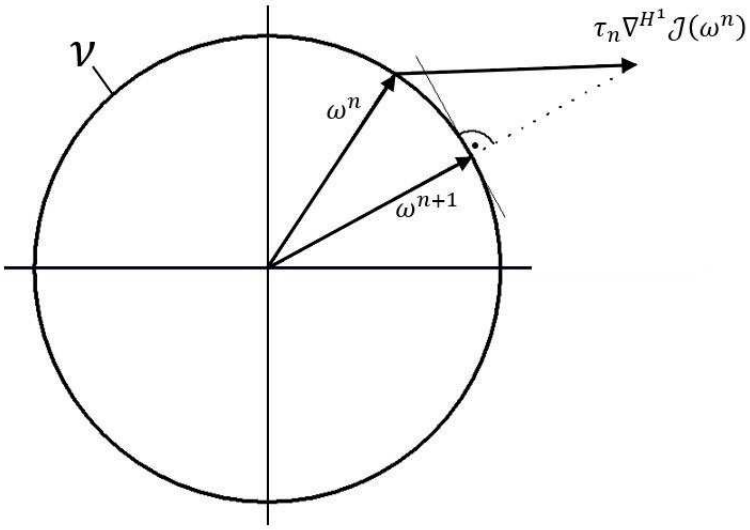

Figure 5: Scheme of the arc optimization of the vorticity field ω over the set $\mathcal{V}$. At every iteration step of the steepest ascent algorithm, the updated vorticity field is projected back onto the circle $\mathcal{V}$.

Because of the nonconvex nature of the optimization problem (29), the proposed algorithm may fail. For certain values of $\mathcal{E}_0$, we observe discontinuous "jumps" in the function $\max\_\mathrm{d}\mathcal{E}/\mathrm{d}t(\mathcal{E}_0)$. Therefore, to reduce the probability of failure, we will utilize the continuation method, in which the optimal vorticity state computed for the initial enstrophy $\mathcal{E}_0 - \Delta\mathcal{E}_0$ will be used as the initial guess for $\mathcal{E}_0$, where $\Delta\mathcal{E}_0$ is some sufficiently small positive real number.

To sum up, in order to compute the maximum enstrophy growth $\mathrm{d}\mathcal{E}/\mathrm{d}t$ for a given $\mathcal{E}_0$, one has to solve the eigenvalue problem (70) and then proceed with the steepest ascent scheme (44) repeatedly for increasing values of $\mathcal{E}_0$ taking into account all the guidelines mentioned in this section. Algorithm 1 clearly outlines the entire optimization proce-

dure. Following the continuation approach, for the initial enstrophy $\mathcal{E}_0 + \Delta\mathcal{E}_0$ one can repeat steps 4-7 of Algorithm 1 using $\omega^n(\mathcal{E}_0)$ as the initial guess ω_*.

Algorithm 1 Input: $\mathcal{E}_0$, Output: max_d$\mathcal{E}$/dt

1. **Solve** eigenvalue problem (70).
2. **Choose** ω_0 from the set of eigenfunctions of (70).
3. **Project** ω_0 onto $\mathcal{V}$.
4. **Set** ε, d$\mathcal{J}$.
5. **Set** n=0.
6. **While** d$\mathcal{J} > \varepsilon$
   - i **Compute** the H^1 gradient $\nabla^{H^1}\mathcal{J}(\omega^n)$ by solving (52), (61) and (63).
   - ii **Compute** τ_n such that
   $$\tau_n = \arg\max_{\tau>0} \mathcal{J}\left(\frac{\omega^n + \tau\nabla^{H^1}\mathcal{J}(\omega^n)}{||\omega^n + \tau\nabla^{H^1}\mathcal{J}(\omega^n)||_{L_2}}\mathcal{E}_0\right),$$
   using Brent's method.
   - iii $\omega^{n+1} = \omega^n + \tau\nabla^{H^1}\mathcal{J}(\omega^n)$.
   - iv **Project** ω^{n+1} onto $\mathcal{V}$.
   - v $\Delta\mathcal{J} = (\mathcal{J}(\omega^{n+1}) - \mathcal{J}(\omega^n))/\mathcal{J}(\omega^n)$.
   - vi $\omega^n = \omega^{n+1}$.
   - vii $n = n + 1$.
7. max_d$\mathcal{E}$/d$t := \mathcal{J}(\omega^n)$.

5 Computational Results

In this chapter, all computational results, grouped in three categories, will be presented. Firstly, we will validate the computations, which means that we will check their accuracy by performing convergence test of certain quantities with respect to different parameters, such as the resolution parameter N, number of iterations in the steepest ascent algorithm, etc. Secondly, eigenfunctions of (70) corresponding to the first six leading eigenvalues will be illustrated. Finally, we will focus on the central part of this thesis, namely the maximum instantaneous enstrophy growth and the corresponding extreme states of the vorticity. In all numerical experiments, the viscosity parameter ν is fixed and equals to 1, while the tolerance number ε (vide Algorithm 1) is 10^{-10}. In most numerical examples, two sets of the results will be presented, one corresponding to the square domain whose lenght/width is 2 , and the other to the circular domain with the radius 1. In section 5.3, we will use the phrase "the nth branch" which refers to the relation between the maximum enstrophy growth and the initial enstrophy $\mathcal{E}_0$, where the extreme states converge to the nth eigenfunction of (70) as $\mathcal{E}_0 \to 0$. The quantity of maximum enstrophy growth will be simply denoted as $\max\_\mathrm{d}\mathcal{E}/\mathrm{d}t$.

5.1 Validation

Our first numerical experiment is to investigate the convergence of the eigenvalues of (70) with respect to the resolution parameter N on the square domain. Figure 6 illustrates the behaviour of the relative error corresponding to the four leading eigenvalues, on linear-logarithmic scale. This type of axis scaling enables us to examine if the method exhibits the spectral convergence. We observe that the error decay is not as fast as the

one in Figure 3, which is a consequence of the matrix modification described in section 4.2. In the case of the circular domain, the convergence rate of the relative error is comparable to the one in Figure 3.

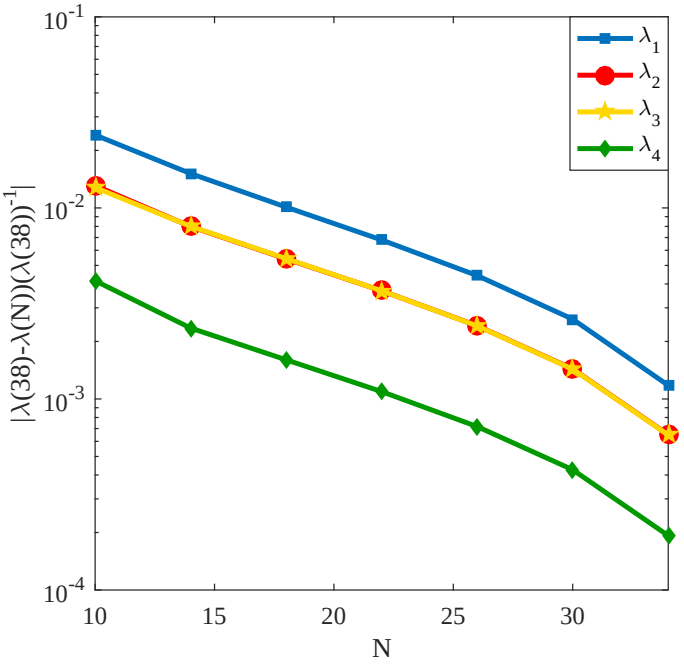

Figure 6: Relation of the relative error correspoding to the first four eigenvalues of (70) with respect and the resolution parameter N on the square domain. Each branch corresponds to a different eigenvalue.

Another test involves the behaviour of max_d$\mathcal{E}/$dt with respect to the number of iterations n. Figure 7 depicts six branches, each corresponds to a different value of the enstrophy $\mathcal{E}_0$. The quantity $\Delta\mathcal{J}$ marked on the vertical axis is defined in Algorithm 1. A careful analysis of all the branches leads to the conclusion that for higher values $\mathcal{E}_0$, one needs more iterations to obtain the desired accuracy. On the other hand, for smaller values of $\mathcal{E}_0$, after only very few iterations we obtain a solution with the machine precision.

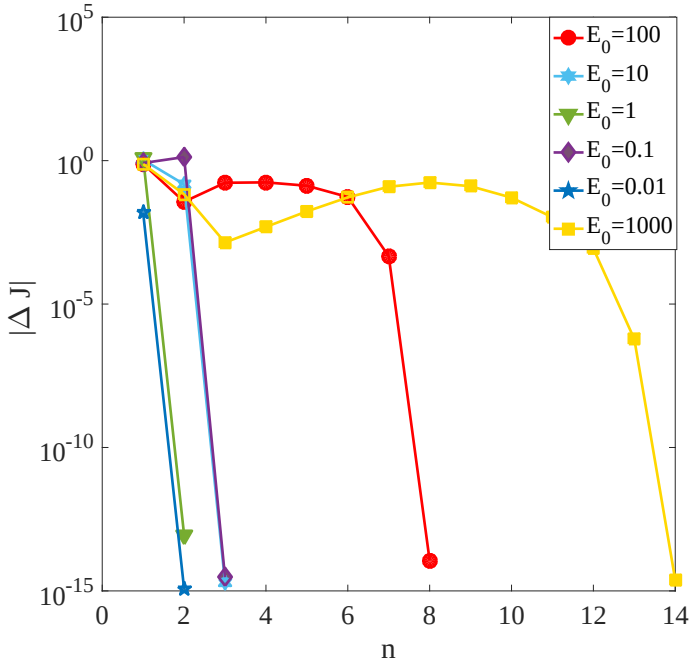

Figure 7: Relation of the absolute value of $\Delta\mathcal{J}$ and the number of iterations n. Each data set corresponds to a different value of $\mathcal{E}_0$.

The final and most important numerical test we would like to perform is the so-called κ-test. It is a reliable tool to verify if the H^1 gradient, which is a central ingredient of the steepest-ascent algorithm, is computed correctly. The κ-test makes use of both the definition of the Gateaux differential (42) and the Riesz representation theorem (46). Thus, given a vorticity field ω and its perturbation ω', we compute the quantity

$$\kappa(\epsilon) = \frac{\epsilon^{-1}(\mathcal{J}(\omega + \epsilon\omega') - \mathcal{J}(\omega))}{\langle \nabla^{H^1}\mathcal{J}(\omega), \omega' \rangle_{H^1}}, \tag{82}$$

as a function of the parameter ϵ. The biggest challenge of the κ-test is to generate both the functions ω and ω', since they must satisfy all the requirements listed in (29). One of the simplest approaches is to solve eigenvalue problem (70) and choose any two eigenfunctions and one of them will serve as the reference state ω, whereas the other one

as the perturbation ω'.

Theoretically, in the limit $\epsilon \to 0$, $\kappa(\epsilon)$ should approach 1. Figure 8 puts together results of two κ-tests performed on both a square and circular domains. Although both experiments involve an equal number of grid points, we observe one significant difference between them. The one corresponding to the circular domain exhibits much better accuracy, the quantity $|\kappa(\epsilon) - 1|$ is at least two orders of magnitude lower than the analogous result for the square domain.

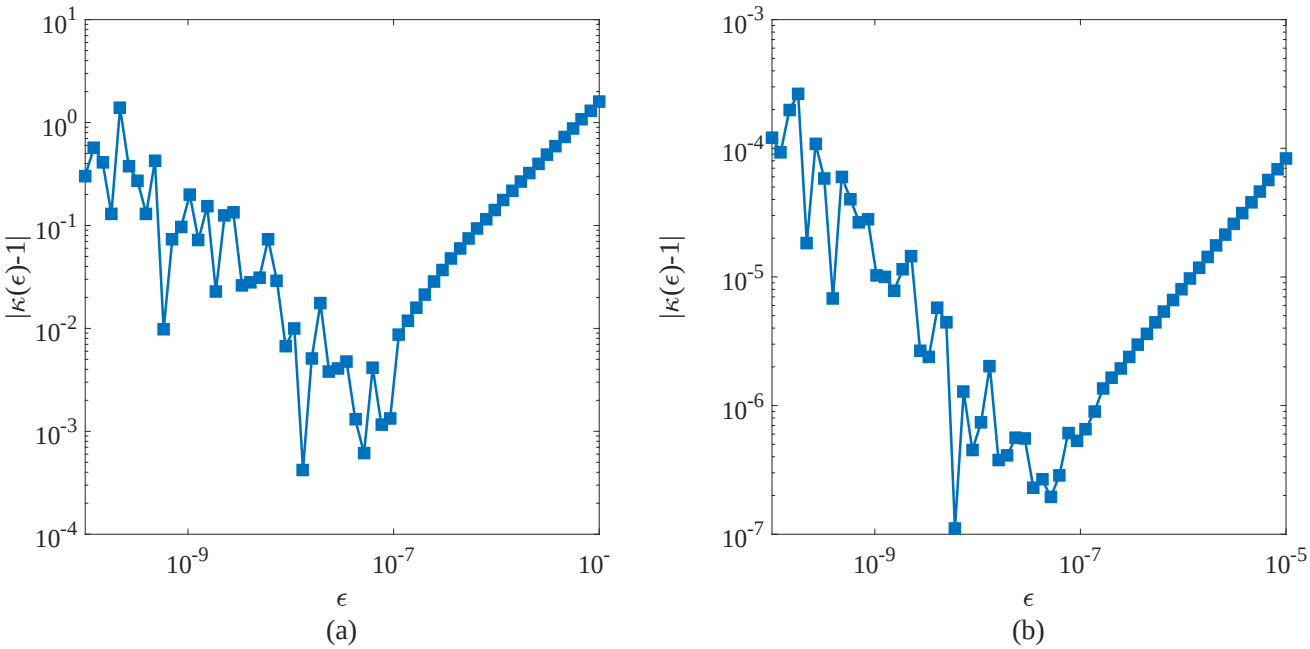

Figure 8: Comparison of the results of two κ-tests performed on a square domain (left) and circular domain (right). Both domains involve the same numbers of grid points. The quantity $|\kappa(\epsilon) - 1|$, marked on the vertical axis, reflects the order of magnitude of the numerical error. In both cases, we selected the second and third eigenfunction of problem (70) that were used ad ω and ω' in (82).

Despite the mentioned difference between the two plots in 8, there are a few common features. We observe that in both cases the error is large for very small values of ϵ. This is a clear consequence of the round-off errors that dominate when $\epsilon < 10^{-8}$. For bigger

values of ϵ, on the other hand, the truncation error prevails leading to significant errors when $\epsilon > 10^{-6}$.

5.2 Numerical Solution of Eigenvalue Problem (70)

According to Algorithm 1, in order to initiate the steepest ascent algorithm one has to solve eigenvalue problem (70) first, since an initial guess is needed. As shown in section 3.3, the set of eigenfunctions of (70) is a good approximation of the solution of optimization problem in the limit $\mathcal{E}_0 \to 0$. Moreover, the eigenvalue problem provides proper candidates for the κ-test.

Figures 9 and 10 illustrate the eigenfunctions corresponding to the leading six eigenvalues, computed on the square an circular domains. All the eigenvalues are both real and positive, which is consistent with the analysis of the algebraic properties of (70) in Appendix A. We observe that the eigenfunctions associated with larger eigenvalues exhibit higher variability in space. In Figure 9, we can distinguish two different arrangements of the vortex cells, aligned and rotated with respect to the domain. A similar observation was highlighted in [1], where Ayala and Protas studied an analogous problem on a periodic domain for small palinstrophies. As noted in the captions of Figures 9 and 10, there exist eigenvalues with the algebraic multiplicity of two (and the geometric multiplicity of one), and their corresponding eigenfunctions are related via a rotation symmetry. All the eigenfunctions are normalized, such that the constraint (70g) is satisfied.

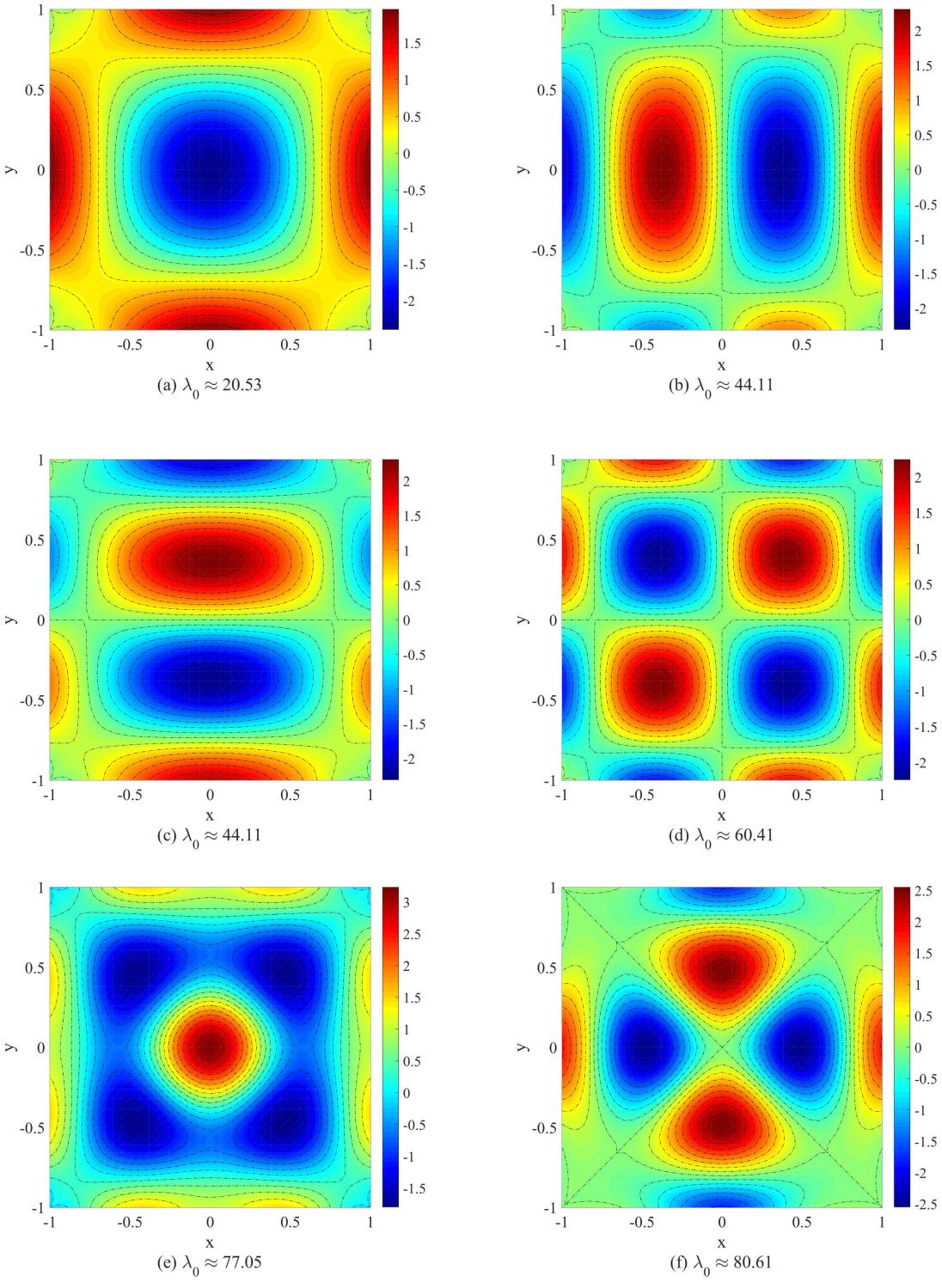

Figure 9: Illustration of eigenfunctions associated with the six leading eigenvalues on the square domain. Their corresponding eigenvalues (truncated to the hundredth decimal number) are: (a) 20.53, (b) 44.11, (c) 44.11, (d) 60.41, (e) 77.05 and (f) 80.61.

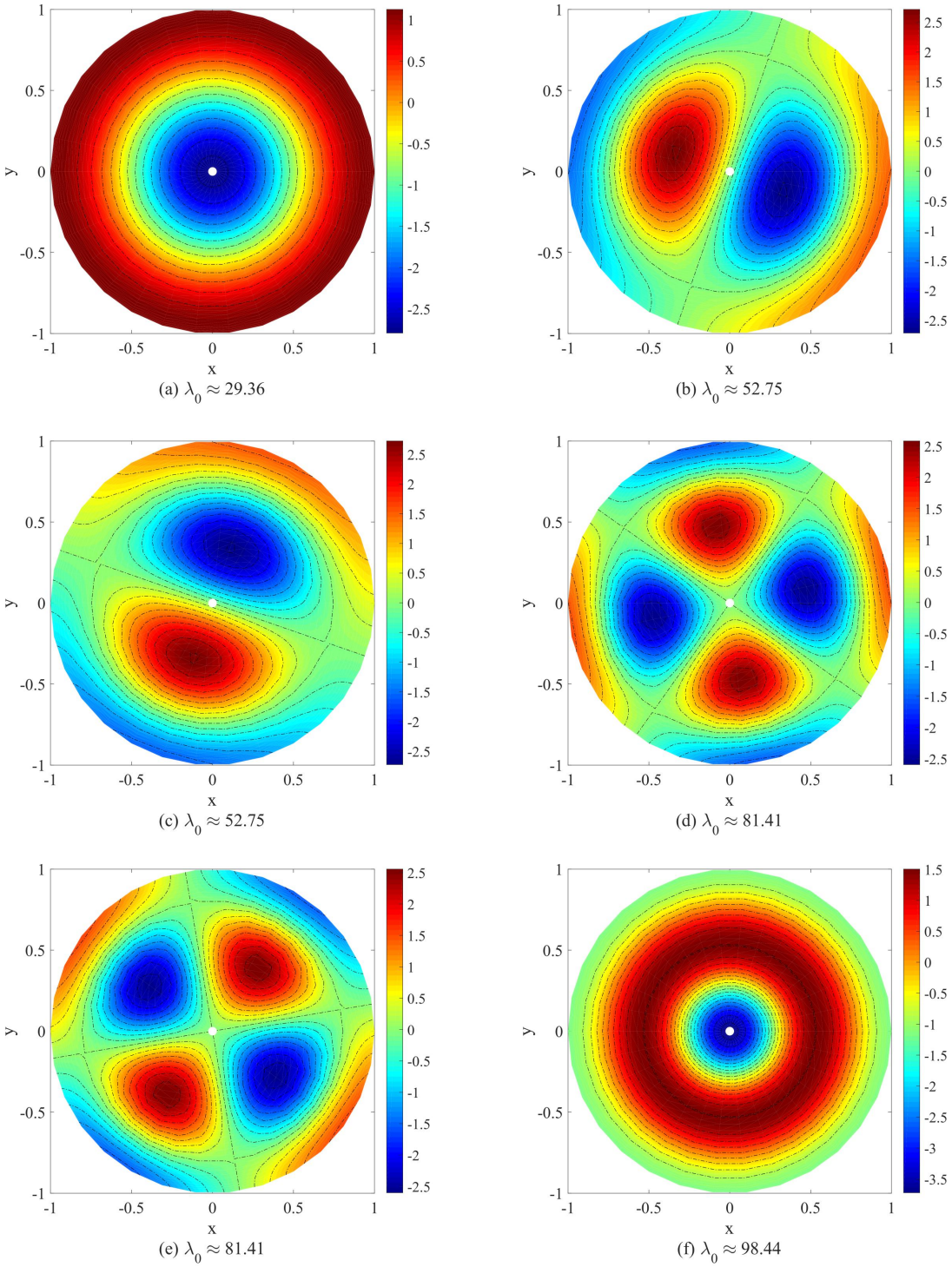

Figure 10: Illustration of eigenfunctions associated with the six leading eigenvalues on the circular domain. Their corresponding eigenvalues (truncated to the hundredth decimal number) are: (a) 29.36, (b) 52.75, (c) 52.75, (d) 81.41, (e) 81.41 and (f) 98.44.

5.3 Maximum Instantaneous Enstrophy Growth and Extreme Vortex States

The final section of this chapter is devoted to the numerical results that have been generated using Algorithm 1. This procedure enables us to compute the maximum instantaneous enstrophy growth for the given value of enstrophy $\mathcal{E}_0$, as well as the corresponding extreme vortex states. Figure 11 depicts a typical dependence of the maximum enstrophy growth and intermediate values of $\mathcal{E}_0$. We can distinguish two distinct regimes, **I** and **II**, where max_d$\mathcal{E}/$dt decreases and increases, respectively. This is a similar behaviour to what we can observe in the work of Protas and Ayala [1].

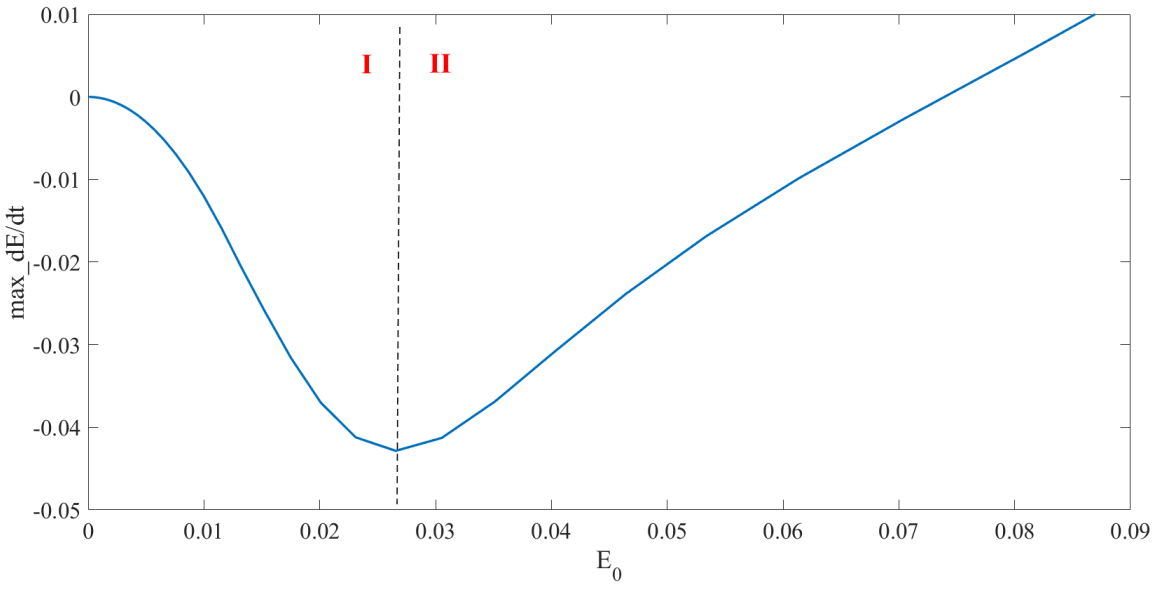

Figure 11: Typical dependence of the maximum enstrophy growth max_d$\mathcal{E}/$dt on $\mathcal{E}_0$ for moderate values of the enstrophy . In this plot, we can distinguish two distinct behavioral regimes: (**I**), when the function is decreasing and (**II**), when we observe an increasing tendency. This is the fourth branch and corresponds to the square domain.

The dependence of max_d$\mathcal{E}/$dt on $\mathcal{E}_0$ for small enstrophy values obtained for five different maximizing branches is presented in Figures 12(a) and 12(b) for the square and circular domain, respectively.

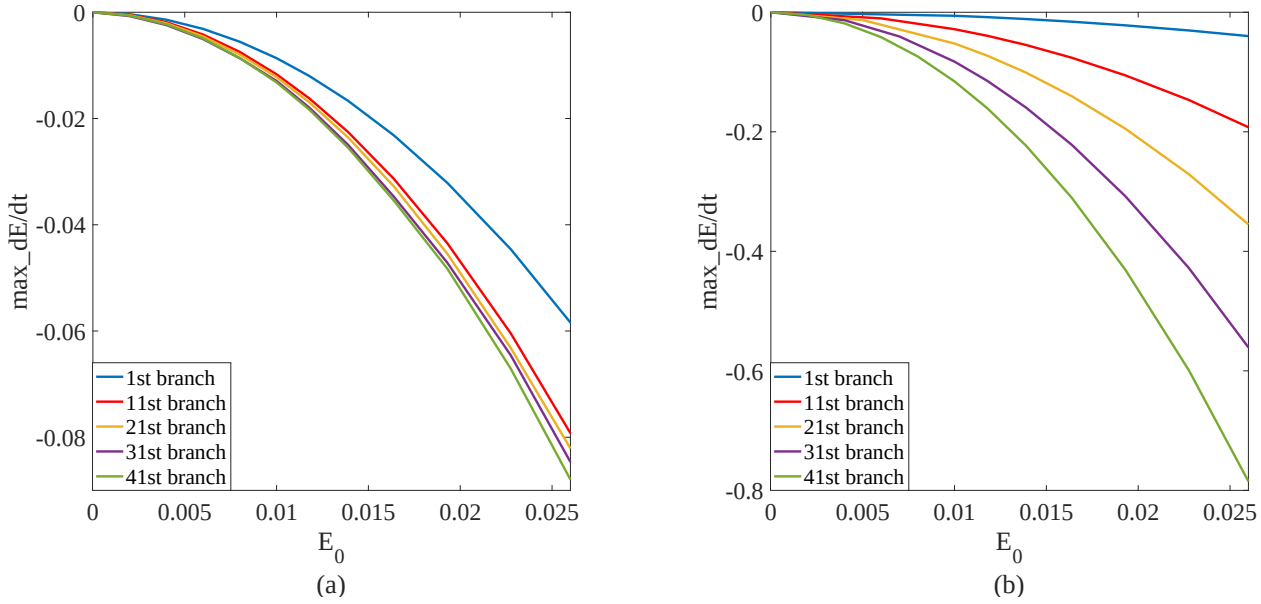

Figure 12: Dependence of the maximum enstrophy growth max_d$\mathcal{E}$/dt on $\mathcal{E}_0$ for small values of the enstrophy. The plot contains five different branches, on both the square (a) and circular (b) domains. Their continuation, for large values of $\mathcal{E}_0$ is presented in Figure 13.

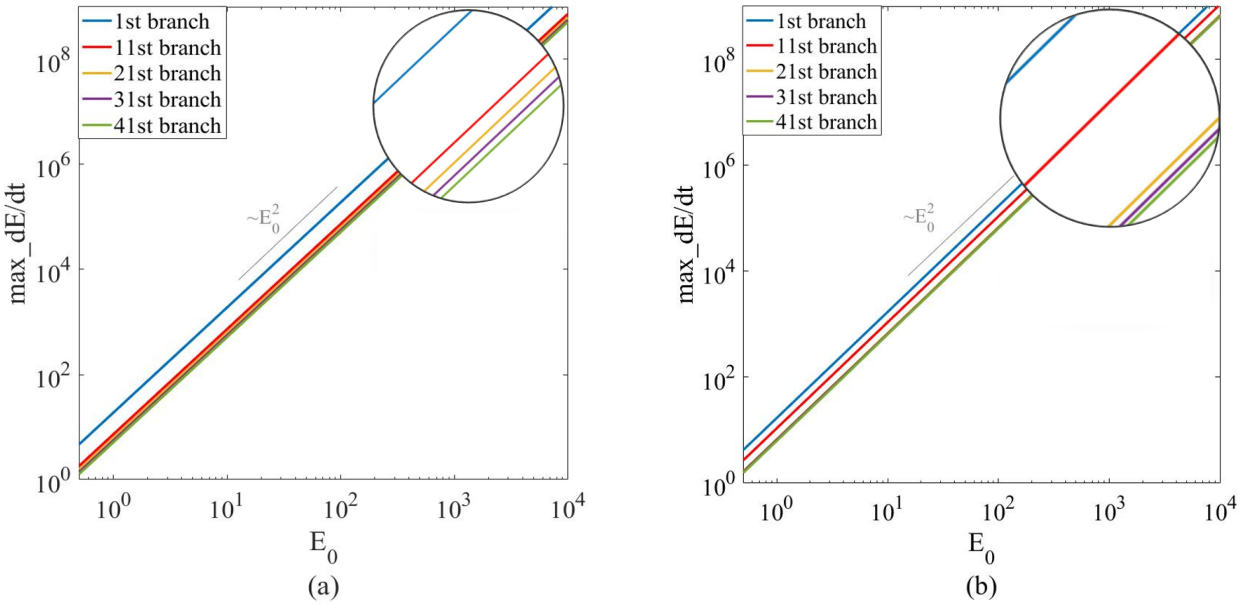

Figure 13: Dependence of the maximum enstrophy growth max_d$\mathcal{E}$/dt on $\mathcal{E}_0$ for large values of the enstrophy. The plot contains five different branches, on both the square (a) and circular (b) domains. Their continuation, for small values of $\mathcal{E}_0$ is presented in Figure 12. An upper part of these branches is zoomed in (in the circle), so we could see their relative arrangement.

It is clear that in the limit $\mathcal{E}_0 \to 0$ the branches corresponding to larger eigenvalues are characterized by smaller values of $\max\_\mathrm{d}\mathcal{E}/\mathrm{d}t$. However, what distinguishes the two plots in Figure 12 is the fact that on the circular domain $\max\_\mathrm{d}\mathcal{E}/\mathrm{d}t$ decreases much faster (even one order of magnitude). Analogously, Figure 13 depicts the continuation of the same branches for high values of $\mathcal{E}_0$, on a logarithmic scale. It features five parallel lines with the slope 2. We can notice that the relative arrangement of these branches is exactly the same as in Figure 12. The final question we would like to address in this thesis is: how do the corresponding extreme vortex states look like? We visualize approximation of $\tilde{\omega}$, obtained in the steepest ascent method (44). Figures 14-16 present six extreme vortex states on the square domain corresponding to the first, fourth and fifth branch, thanks to which we can observe how the extreme states change as $\mathcal{E}_0$ increases. A characteristic feature of the extreme states with large enstrophys is the fact that large vortices appear at all four corners, whereas no structures are visible in the center of the domain. We observe a similar behaviour in Figures 17-18, which illustrate the extreme vortex states on the circular domain, for different values of $\mathcal{E}_0$. Finally, Figure 19 juxtaposes extreme vortex states in the limit $\mathcal{E}_0 \to 0$ with those corresponding to a higher value of $\mathcal{E}_0$. We notice that all the vortices tend to congregate at the boundary, while the number of the vortices strictly depends on the frequency of the oscillations of the initial guess ω_*. Regardless of the type of a domain, the extreme states corresponding to low values of $\mathcal{E}_0$ do not deviate much, from the qualitative point of view, from the eigenfunctions of (70). The majority of presented vortex states are highly symmetric, which a consequence of two facts: first, we consider symmetric domains only (i.e., a square and a unit circle) and, second, vorticity equation (12) does not involve any terms that might affect this property. A few vorticity optimizers, for example (b)-(f) in Figure 17 or (b) in Figure 19, do not exhibit this feature, which is a result of insufficient grid resolution.

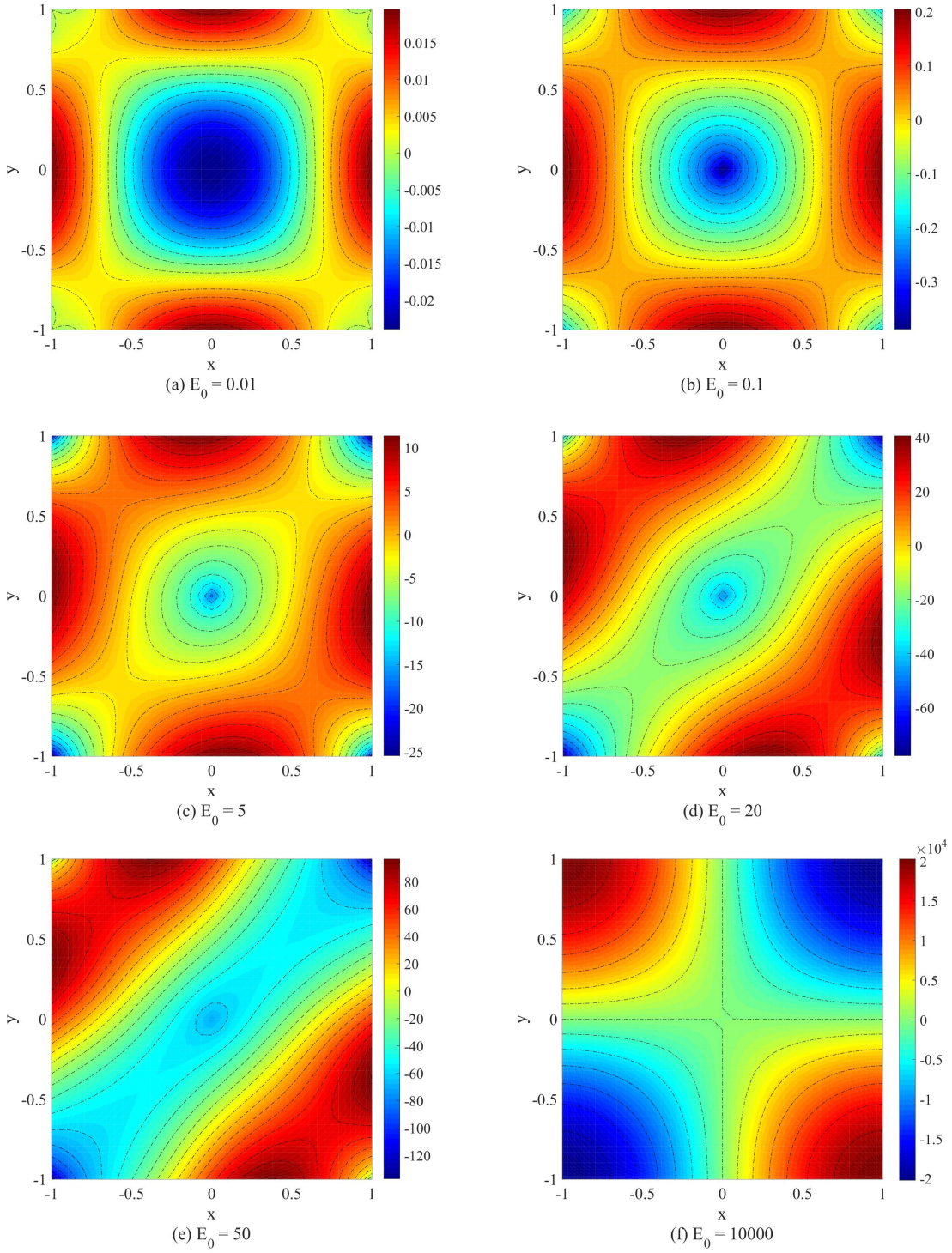

Figure 14: Extreme vortex states associated with the first branch, on the square domain. The illustrated optimizers correspond to the following values of the initial enstrophy $\mathcal{E}_0$: (a) 0.01, (b) 0.1, (c) 5, (d) 20, (e) 50 and (f) 10000.

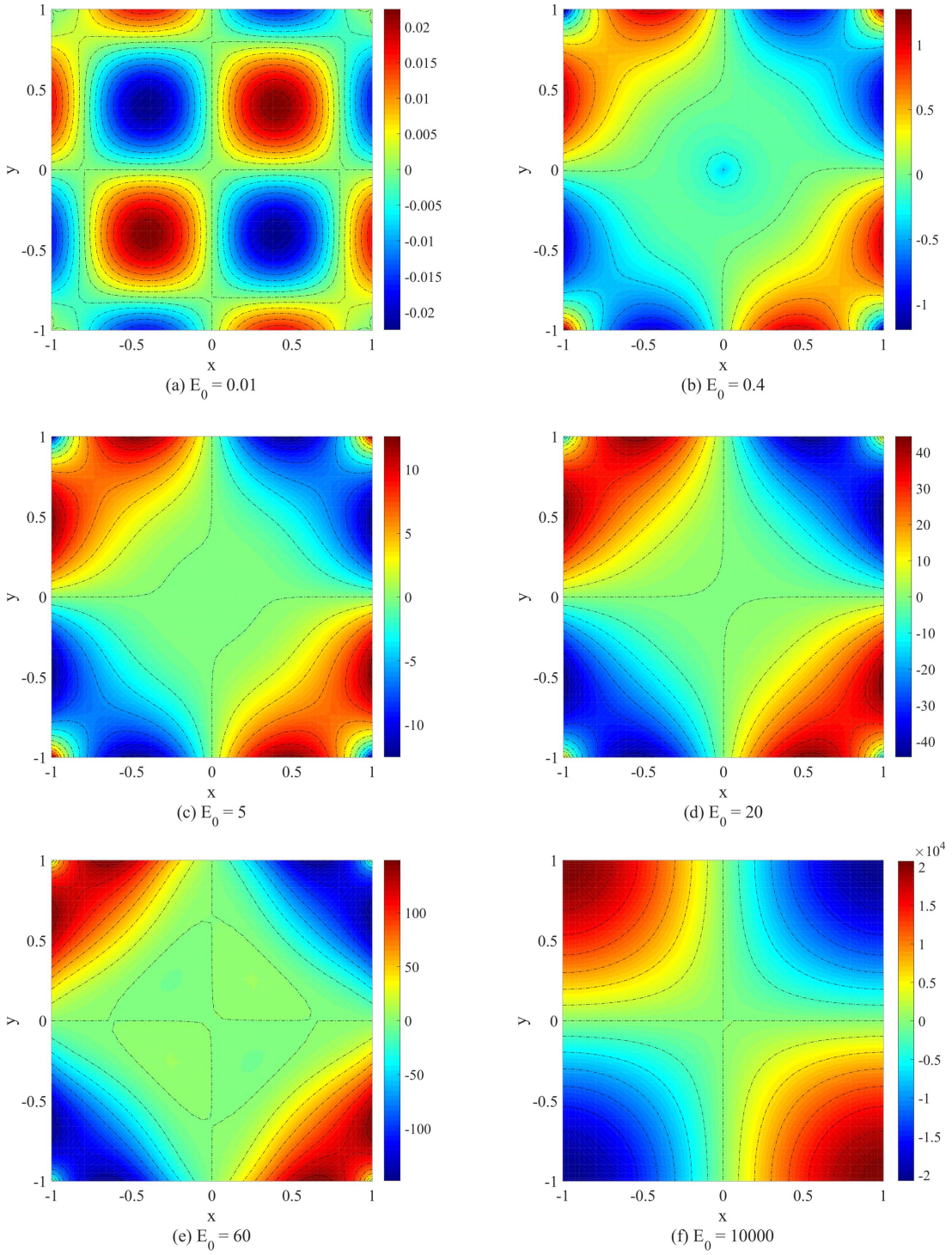

Figure 15: Extreme vortex states associated with the fourth branch, on the square domain. The illustrated optimizers correspond to the following values of the initial enstrophy $\mathcal{E}_0$: (a) 0.01, (b) 0.4, (c) 5, (d) 20, (e) 60 and (f) 10000.

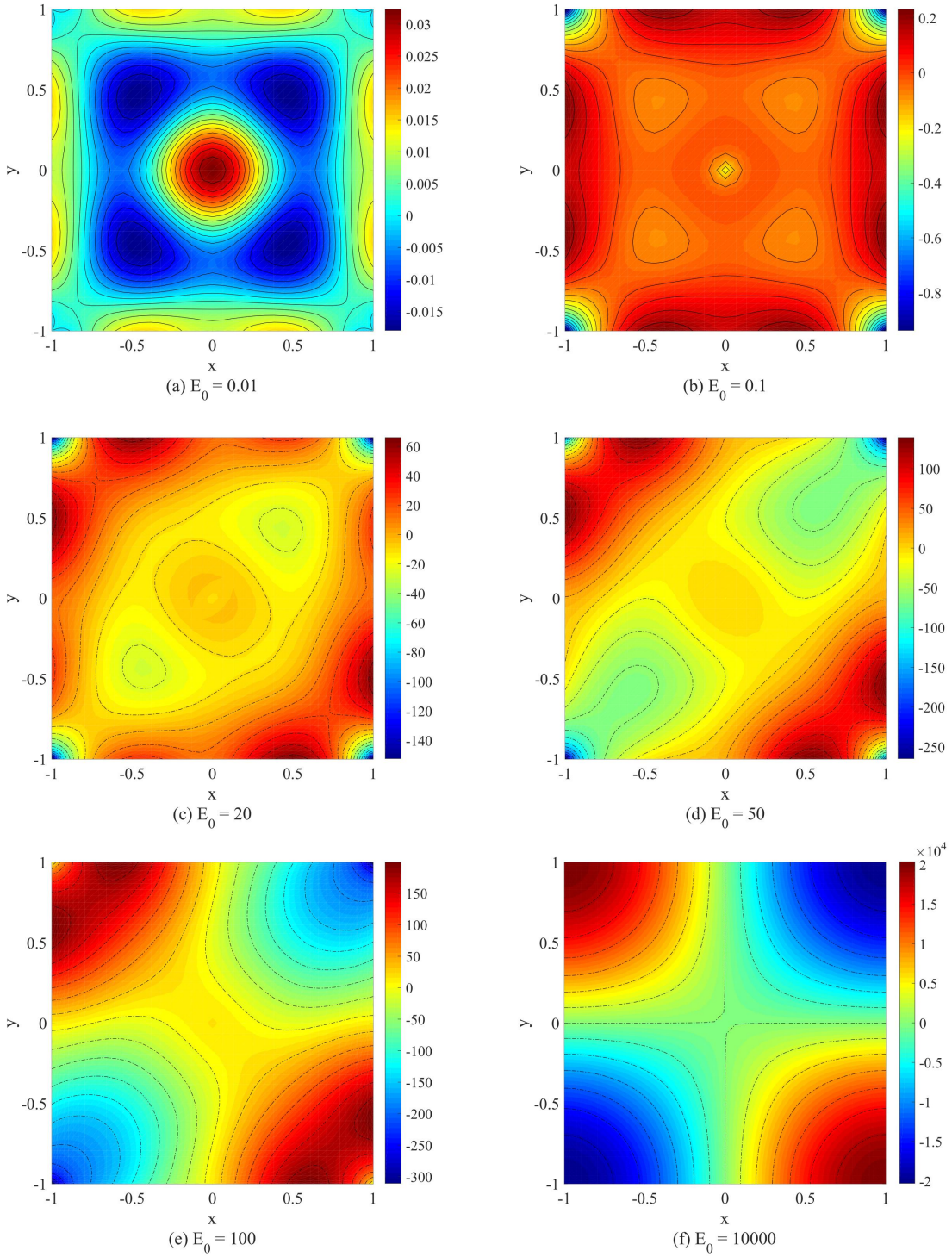

Figure 16: Extreme vortex states associated with the fifth branch, on the square domain. The illustrated optimizers correspond to the following values of the initial enstrophy $\mathcal{E}_0$: (a) 0.01, (b) 0.1, (c) 20, (d) 50, (e) 100 and (f) 10000.

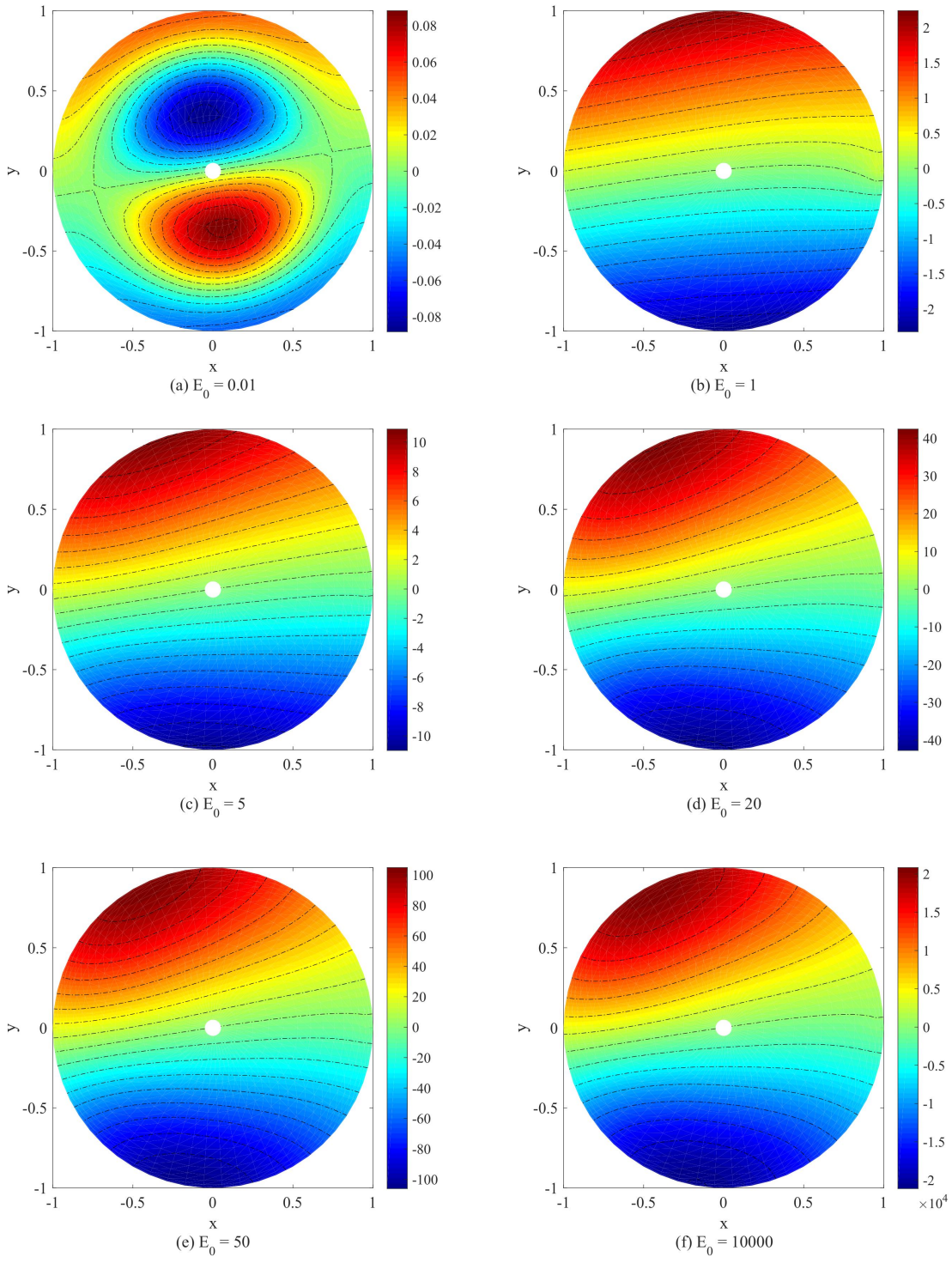

Figure 17: Extreme vortex states associated with the second branch, on the square domain. The illustrated optimizers correspond to the following values of the initial enstrophy $\mathcal{E}_0$: (a) 0.01, (b) 1, (c) 5, (d) 20, (e) 50 and (f) 10000.

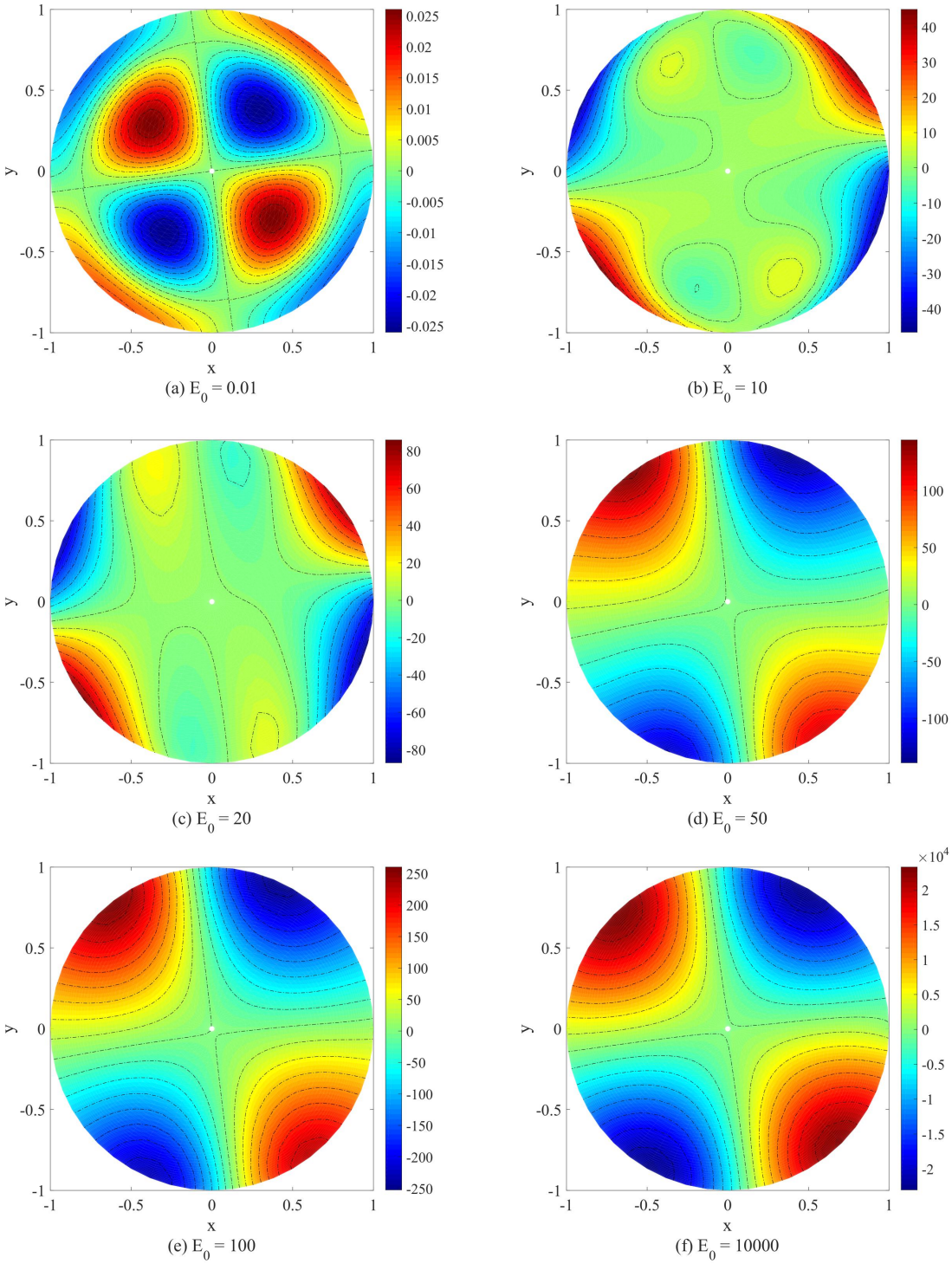

Figure 18: Extreme vortex states associated with the fifth branch, on the circular domain. The illustrated optimizers correspond to the following values of the initial enstrophy $\mathcal{E}_0$: (a) 0.01, (b) 10, (c) 20, (d) 50, (e) 100 and (f) 10000.

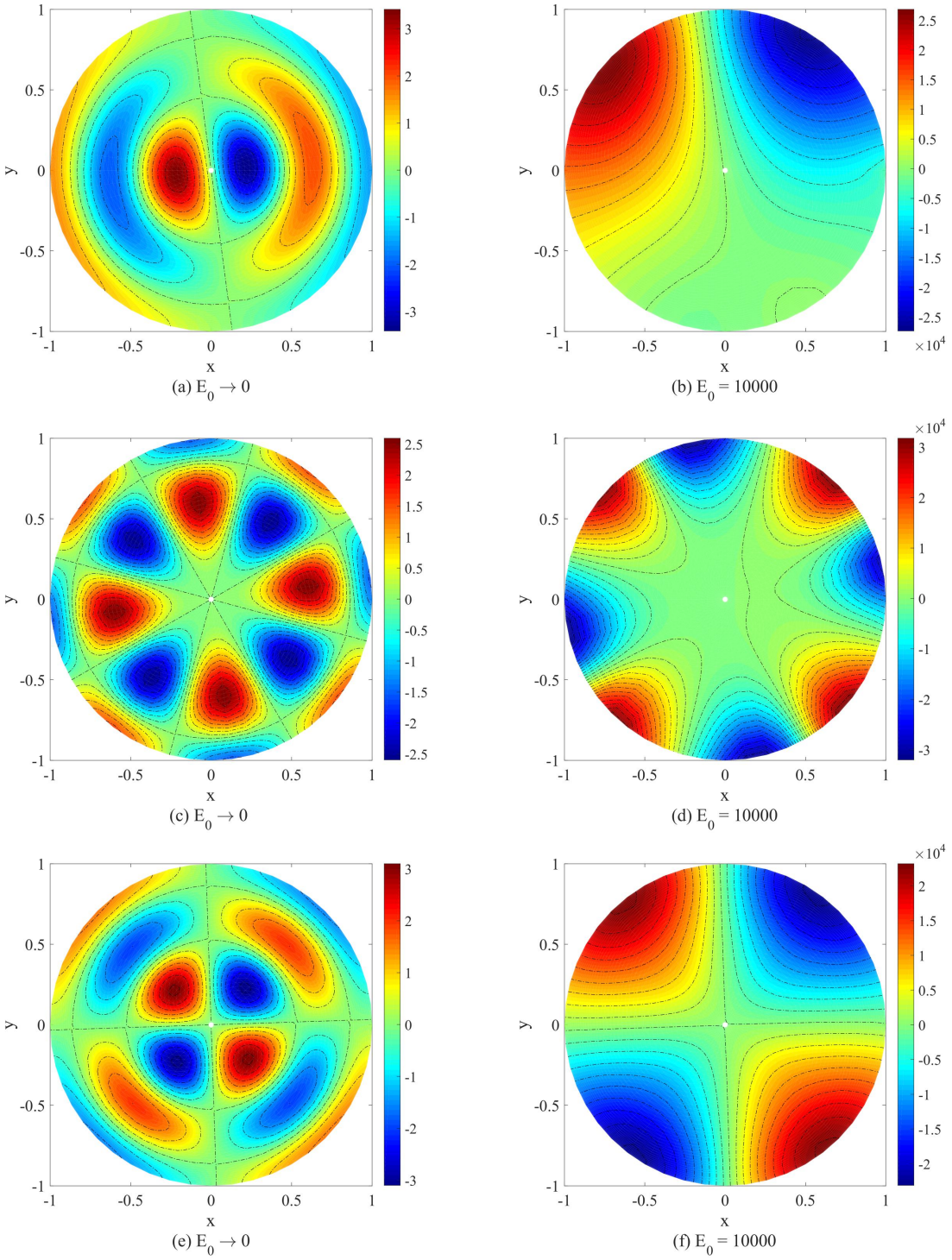

Figure 19: Extreme vortex states associated with the ninth ((a) and (b)), tenth ((c) and (d)), and fourteenth branch ((e) and (f)), on the circular domain. Pictures (a), (c), (e) correspond to the limit $\mathcal{E}_0 \to 0$, while pictures (b), (d), (f), to $\mathcal{E}_0 = 10000$.

6 Final Remarks

In this thesis we proposed an efficient computational approach to find the instantaneous maximum enstrophy growth in the 2D Navier-Stokes system with respect to the initial enstrophy $\mathcal{E}_0$. To achieve our ultimate goal, we utilized the gradient-based method, which is a simple numerical tool useful for optimization problems. The biggest challenge of this project, however, was to find the H^1 gradient $\nabla^{H^1}\mathcal{J}(\omega)$ of objective functional (28). We had to pay close attention to the fact that the H^1 gradient itself must satisfy all constraints listed in (29). Moreover, we aimed to develop a method that is relatively easy to implement. Thanks to the meticulous analytical calculations in Chapter 3, we managed to derive the H^1 gradient satisfying all requirements. The proposed method is based on numerical computations involving simple elliptic-type problems. Finally, this procedure is incorporated in steepest-ascent algorithm (44) enabling us to characterize the maximum instantaneous enstrophy growth. In addition to that, using formal series expansions, we derived eigenvalue problem (70) that corresponds to the solution of optimization problem (29) in the limit $\mathcal{E}_0 \to 0$. Solving (70), we can analyse the behaviour of the maximum enstrophy growth for small values of $\mathcal{E}_0$ and we also provide a proper initial guess (satisfying all constraints) for the steepest-ascent procedure. Another advantage of the gradient-based method is the fact that it prevents us from the direct coding of elliptic operators, such as those appearing in system of Euler-Lagrange equations (41). To program the Green's function, for instance, we would have to apply sophisticated numerical methods to handle the problem of the singularity.

Algorithm 1 shows all the steps required to compute the instantaneous enstrophy growth numerically. To discretize all differential operators in space, we used spectral methods

that guarantee spectral accuracy. Nevertheless, this accuracy is not always achieved due to different numerical interventions, such as the deletion of corner nodes required to desingularize the matrix in the case of square domains. To accelerate the steepest-ascent algorithm, we employed Brent's method that turns out be very simple to implement. It reduces the number of iterations to just a few, which makes the whole procedure computationally efficient.

The core question we asked at the beginning of this study is how much enstrophy a flow can produce on a bounded domain. Figures 11,12 and 13 answer this question and also show that the maximum enstrophy growth can be described as,

$$\frac{\mathrm{d}\mathcal{E}}{\mathrm{d}t} = C_n \mathcal{E}_0^2 \quad \text{for} \quad \mathcal{E}_0 \to \infty, \tag{83}$$

or, alternatively, using the Reynolds number Re_0 corresponding to $\mathcal{E}_0$,

$$\frac{\mathrm{d}\mathcal{E}}{\mathrm{d}t} = \tilde{C}_n Re_0^4 \quad \text{for} \quad Re_0 \to \infty, \tag{84}$$

where both $C_n > 0$ and $\tilde{C}_n > 0$ denote constants associated with the nth branch. These constants decrease as n gets bigger. The above observation is consistent with the statement that there is no blow-up in the 2D Navier-Stokes system. Moreover, the numerical result affirms another statement, namely that the H^1 topology is sufficient in the study of the boundedness of the maximum enstrophy growth on 2D bounded domains.

All numerical experiments were performed on both the square and circular domains to investigate if the shape has any impact on the results. It turned out that there are some minor differences. One of them can be found in Figure 12, where we observe that for small $\mathcal{E}_0$'s, the values of the maximum enstrophy growth tend to be much smaller (by even one order of magnitude) on the circular domain than the corresponding values

on the square domain. Another difference involves the extreme states of the vorticity. In the case of circular domains, for big values of $\mathcal{E}_0$, all vortices tend to cluster at the boundary, while their total number depends on the branch index. On the square domain, however, there always appear four vortices, one at each corner, regardless on the branch number. Based on simple algebraic manipulations, we also conclude that the solutions of eigenvalue problem (70) on the circular domain are separable, which means that they can be written as a product of two independent functions, e. g.

$$\omega_1(r, \theta) = R_1(r)T_1(\theta), \tag{85}$$

where T_1 is a simple trigonometric function, while R_1 belongs to the family of Bessel functions. This characteristic is clearly visible in Figure 10 and resembles the one in the 2D Stokes system. Another aspect we would like to highlight is the fact that on the circular domain there exists a continuous family of eigenfunctions parametrized by an arbitrary rotation angle. It means that if we rotate the solution presented in 10 by an arbitrary angle, the obtained vorticity field will still be a solution of eigenvalue problem (70). The orientation of all function maps on the circular domain strictly depends on the method of spatial discretization.

There exist a few analogies between our results and those presented by Ayala and Protas (in [1]), who performed a similar study on periodic domains. First of all, the solutions of the optimization problem in the limit $\mathcal{E}_0 \to 0$, as shown in Figures 9 and 10, exhibit two types of vortex arrangements, aligned and rotated with respect to the domain. Moreover, the relation between the maximum enstrophy growth and the initial enstrophy $\mathcal{E}_0$ (vide Figure 11) features two distinct regimes; first, for small values of $\mathcal{E}_0$ when the function decreases and, second, corresponding to moderate and large values of $\mathcal{E}_0$ when it increases.

Although this project is considered to be very successful, both from the mathematical and numerical points of view, there are still a lot of aspects that should be further analysed. There is still a shortage of rigorous mathematical proofs or estimates involving cases with bounded domains. It means that at present none of the results presented in Chapter 5 can be supported by corresponding analytical estimates. Furthermore, an analogous analysis in the three-dimensional space would provide us an insight into the enstrophy production process in the 3D space. Lastly, it is desirable to improve certain parts of Algorithm 1, to make it even more computationally efficient. The biggest limitation of the proposed procedure is the fact that it is sometimes complicated to compute a full branch of the relation $\max\_\mathrm{d}\mathcal{E}/\mathrm{d}t$ vs. $\mathcal{E}_0$ (vide Figure 11 or 13). Since the optimization problem (29) is nonconvex, in the actual continuation process we observe characteristic discontinuous "jumps" from one branch to another and sometimes it is required to manually refine the $\mathcal{E}_0$ grid to avoid this phenomenon. Therefore, the process of generating a branch requires a few numerical attempts or, sometimes, it is recommended to apply the backward continuation technique. A full automation of the branch generating procedure would certainly save our time.

This thesis is focused on the methodology enabling us to optimize the maximum enstrophy growth in the 2D Navier-Stokes system on bounded domains at $t = 0$ only. What do these results imply about solutions for $t > 0$? To answer this question, one would have to modify the proposed technique, which would involve the solution of the vorticity-streamfunction system over time. Another interesting computational tool that might used in the study of the extreme behaviours in the Navier-Stokes system is shape optimization. This approach can be used to find the optimal domain shape on which the cost functional is maximum and all constraints are satisfied. Undoubtedly, these are just two of a few scientific goals for the future, that will help us to better understand the phenomenon of enstrophy production.

A Algebraic Properties of the Linear Operator Associated with (70)

The purpose of this section is to take a closer look at the PDE operator associated with (70), here denoted as $\mathcal{D}$. To shorten the notation, we will denote $\tilde{f} = [\omega, \psi, g, f]^T$. Firstly, we will check if the linear operator is symmetric, which can be proven by showing that the following identity is true:

$$\left\langle \mathcal{D}\tilde{f}_1, \tilde{f}_2 \right\rangle_{L_2} = \left\langle \tilde{f}_1, \mathcal{D}\tilde{f}_2 \right\rangle_{L_2}, \tag{86}$$

where $\tilde{f}_1 = [\omega_1, \psi_1, g_1, f_1]^T$ and $\tilde{f}_2 = [\omega_2, \psi_2, g_2, f_2]^T$. The LHS of (86) will be further denoted as A, while the RHS as B. Therefore, using the equations of (70) and integrating them by parts, we obtain

$$\begin{aligned} A &= \int_\Omega (-2\nu\Delta\omega_1 - g_1)\omega_2 + (-\omega_1 - \Delta\psi_1)\psi_2 - \Delta g_1 g_2 - \Delta f_1 f_2 \mathrm{d}\Omega \\ &= \int_\Omega (-2\nu\Delta\omega_1 - g_1)\omega_2 \mathrm{d}\Omega = \lambda_0 \int_\Omega \omega_1\omega_2 \mathrm{d}\Omega, \end{aligned} \tag{87}$$

and, analogously,

$$\begin{aligned} B &= \int_\Omega (-\Delta\omega_2 - g_2)\omega_1 + (-\omega_2 - \Delta\psi_2)\psi_1 - \Delta g_2 g_1 - \Delta f_2 f_1 \mathrm{d}\Omega \\ &= \int_\Omega (-\Delta\omega_2 - g_2)\omega_1 \mathrm{d}\Omega = \lambda_0 \int_\Omega \omega_2\omega_1 \mathrm{d}\Omega, \end{aligned} \tag{88}$$

which means that

$$A = B, \tag{89}$$

and, therefore, the operator $\mathcal{D}$ is symmetric. This conclusion implies $\mathcal{D}$ admits real eigenvalues only.

Another important aspect that we want to study is the sign-definiteness of $\mathcal{D}$. One can use exactly the same methodology as above to investigate the sign of the following quantity,

$$\left\langle \mathcal{D}\tilde{f}, \tilde{f} \right\rangle_{L_2} = C, \tag{90}$$

which leads to,

$$\begin{aligned} C &= \int_{\Omega} (-\Delta\omega - g)\omega + (-\omega - \Delta\psi)\psi - \Delta g g - \Delta f f \mathrm{d}\Omega \\ &= \int_{\Omega} (-\Delta\omega - g)\omega \mathrm{d}\Omega = \lambda_0 \int_{\Omega} \omega^2 \mathrm{d}\Omega = \lambda_0 \end{aligned} \tag{91}$$

It is now clear that the value of C does not depend on any of the functions in $\tilde{\mathbf{f}}$, but only on the parameter (eigenvalue) λ_0. This observation means that the operator $\mathcal{D}$ is sign-definite.

References

[1] D. Ayala and B. Protas. Maximum Palinstrophy Growth in 2D Incompressible Flows, *Journal of Fluid Mechanics*, 742:340-367, 2014.

[2] D. Ayala and B. Protas. On maximum enstrophy growth in a hydrodynamic system, *Physica D*, 240:1553-1563, 2011.

[3] J. F. Bonnas, J.C. Gilbert, C. Lemarechal and C.A. Sagastizabal. *Numerical Optimization. Theoretical and Practical Aspects*. Springer, 2003.

[4] R. Bwemba and R. Pasquetti. On the influence matrix used in the spectral solution of the 2D Stokes problem (vorticity-streamfunction formulation), *Applied Numerical Mathematics*, 16:299-315, 1995.

[5] U. Ehrenstein and R. Peyret. A Chebyshev Collocation Method for the Navier-Stokes Equations with Application to Double-Diffusive Convection, *International Journal of Numerical Methods in Fluids*, 9:427-452, 1989.

[6] L. C. Evans. *Partial Differential Equations*. American Mathematical Society, 2010.

[7] C. L. Fefferman. Existence and smoothness of the Navier-Stokes equation. available at `http://www.claymath.org/sites/default/files/navierstokes.pdf`, 2000. Clay Millennium Prize Problem Description.

[8] C. Foias and R. Temam. Gevrey class regularity for the solutions of the Navier-Stokes equations. *Journal of Functional Analysis*, 87:359-369, 1989.

[9] B. Fornberg. *A Practical Guide to Pseudospectral Methods*. Cambridge University Press, 1998.

[10] B. Fornberg. A pseudospectral approach for polar and spherical geometries, *SIAM Journal of Scientific Computing*, 16:1071-1081, 1995.

[11] D. Gottlieb, M. Y. Hussaini and S. A. Orszag. *Introduction: Theory and Applications of Spectral Methods*, in R. G. Voigt. D. Gottlieb, and M. Y. Hussaini, eds. Spectral Methods for Partial Differential Equations, SIAM, 1984.

[12] M. D. Gunzburger. *Perspectives in Flow Control and Optimization*, Chapter 2. Advances in Design and Control. SIAM, 2003.

[13] R. A. Horn and C. R. Johnson. *Topics in Matrix Analysis*. Cambridge University Press, 1996.

[14] L. Lu and C. R. Doering. Limits on enstrophy growth for solutions of the three-dimensional Navier-Stokes equations, *Indiana University Mathematics Journal*, 57:2693-2727, 2008.

[15] D. Lueneberger. *Optimization by Vector Space Methods*. John Wiley and Sons, 1969.

[16] G. Luo and T. Y. Hou. Toward the finite-time blowup of the 3D axisymmetric Euler equations: A numerical investigation. *Multiscale Modeling Simulation*, 12:1722-1776, 2014.

[17] Multiprecision Computing Toolbox for MATLAB Advanpix LLC. Yokohama, Japan, 2016.

[18] R. Peyret. *Spectral Methods for Incompressible Viscous Flow*. Springer, 2002.

[19] B. Protas, T. Bewley and G. Hagen. A comprehensive framework for the regularization of adjoint analysis in multiscale PDE systems. *Journal of Computational Physics*, 195:49-89, 2004.

[20] A. Salih. Streamfunction-Vorticity Formulation, Indian Institute of Space Science and Technology, 2013.

[21] E. M. Stein and R. Shakarchi. *Real Analysis. Measure Theory, Integration and Hilbert Spaces*, volume 3 of *Princeton Lectures in Analysis*. Princeton University Press, 2005.

[22] L. N. Trefethen. *Spectral Methods in Matlab*. SIAM, 2000.